

Fault Throw and Regional Uplift Histories from Drainage Analysis: Evolution of Southern Italy

J. Quye-Sawyer¹, A. C. Whittaker¹, G. G. Roberts¹, D. H. Rood¹

¹Department of Earth Science and Engineering, Imperial College London, SW7 2AZ, UK.

This manuscript is a pre-print and has been submitted for publication in *Tectonics*. Please note that, despite having undergone peer-review, the manuscript has yet to be formally accepted for publication. If accepted, the final version of this manuscript will be available via the “Peer-reviewed Publication DOI” link on the right-hand side of this webpage. Please feel free to contact any of the authors directly to comment on the manuscript.

1 **Fault Throw and Regional Uplift Histories from**
2 **Drainage Analysis: Evolution of Southern Italy**

3 **J. Quye-Sawyer¹, A. C. Whittaker¹, G. G. Roberts¹, D. H. Rood¹**

4 ¹Department of Earth Science and Engineering, Imperial College London, SW7 2AZ, UK.

5 **Key Points:**

- 6 • River profile inversion was used to calculate Pleistocene to Recent uplift rates in
7 space and time
8 • Inverse modelling implies throw rate increases for Calabria's major faults
9 • Regional uplift rates appear similar for most of Calabria once faulting is taken into
10 account

Corresponding author: Jennifer Quye-Sawyer, jennifer.quye-sawyer11@imperial.ac.uk

Abstract

Landscapes can record elevation changes caused by multiple tectonic processes. Here, we show how coeval histories of spatially coincident normal faulting and regional uplift can be deconvolved from river networks. We focus on Calabria, a tectonically active region incised by rivers, many of which contain knickpoints. Marine fauna indicate that Calabria has been uplifted by >1 km since approximately 0.8–1.2 Ma, which was used to calibrate parameters in a stream power erosional model. To deconvolve the local and regional uplift contributions to topography, we performed a spatio-temporal inversion of 994 fluvial longitudinal profiles. Uplift rates from fluvial inversion replicate the spatial trend of rates derived from dated Mid–Late Pleistocene marine terraces, and the magnitude of predicted uplift rates matches the majority of marine terrace uplift rates. We used the predicted uplift history to analyse long-term fault throw, and combined throw estimates with ratios of footwall uplift to hanging wall subsidence to isolate the non-fault related contribution to uplift. Increases in fault throw rate—which may suggest fault linkage and growth—have been identified on two major faults from fluvial inverse modelling, and total fault throw is consistent with independent estimates. The temporal evolution of non-fault related regional uplift is consistent for three locations. Our results may be consistent with toroidal mantle flow generating uplift, perhaps if faulting reduces strength of the overriding plate. In conclusion, fluvial inverse modelling can be an effective technique to quantify fault array evolution, and can deconvolve different sources of uplift that are superimposed in space and time.

1 Introduction

The evolution of normal faults has important implications for long-term seismic hazard, and changes in topography during the development of a fault array impact upon a range of factors, including plate rheology and sediment routing (e.g. Li et al., 2016; Marc et al., 2016; Cowie et al., 2017). Techniques such as trenching and cosmogenic dating of fault scarps can constrain fault throw rates over timescales of $\sim 10^2$ – 10^3 years and can successfully estimate earthquake recurrence intervals (e.g. Pantosti et al., 1993; G. P. Roberts & Michetti, 2004; Cowie et al., 2017). Fault throw over longer timescales ($>10^3$ years) can be investigated using stratigraphic data and structural cross sections (e.g. Mirabella et al., 2011; Ford et al., 2013; Shen et al., 2017), however the temporal and spatial record of throw rates may be limited by the absence of datable stratigraphy. Fortunately, fluvial networks provide an opportunity to overcome these limitations and constrain throw rate on the length and timescales that may be pertinent to the development of a fault array, i.e. $\sim 10^2$ – 10^5 m and $\sim 10^4$ – 10^7 years (e.g. Cowie et al., 2000; McLeod et al., 2000). Quantitative fluvial erosion models can elucidate tectonic changes without necessarily relying upon the stratigraphic archive, signifying their importance in terrestrial settings where fluvial landscapes are ubiquitous at low–mid latitudes. The morphology and erosion rates of individual rivers have been used to confirm the location of active faults, estimate increases in throw rate, and understand fault interaction or relay ramp development (e.g. Commins et al., 2005; Hopkins & Dawers, 2015). These studies have successfully shown that drainage morphology is sensitive to the evolution of individual fault strands. Nonetheless, active faulting rarely occurs in isolation from other tectonic processes (e.g. mantle flow, plate flexure, isostatic rebound), which often modify topography over larger spatial scales (e.g. 10^5 m). Therefore, separating the effect of faulting from the other factors that generate topography remains a wider challenge in tectonic and geomorphic research.

1.1 Spatial scales of uplift and geomorphic response

Observational and theoretical studies have demonstrated the influence of tectonic perturbations on the morphology of fluvial networks (e.g. Howard, 1994; Stock & Montgomery, 1999). In particular, longitudinal profiles (i.e. channel elevation as a function

of downstream distance) usually exhibit a transient response to changes in uplift rate in the form of breaks in slope, known as knickpoints (e.g. Whipple & Tucker, 1999; Kirby & Whipple, 2012). Rivers are particularly useful for tectonic analysis because, for a particular upstream area, higher uplift rates produce steeper channel slopes (assuming constant sediment cover, precipitation etc.), therefore spatial differences in uplift magnitude may be observed directly from the landscape (e.g. Kirby & Whipple, 2012; Whittaker, 2012). Second, river erosion in detachment-limited settings is dominantly an advective process. As the wave of erosion travels upstream through time (assuming erosion rate is linearly proportional to channel slope) the river contains a record of past uplift events (e.g. Loget & Van Den Driessche, 2009; Pritchard et al., 2009; G. G. Roberts & White, 2010).

Changes in uplift rate estimated from river profiles have been used to examine causative tectonic processes such as active faulting, fold growth or dynamic topography (e.g. Kirby & Whipple, 2001; G. G. Roberts & White, 2010; Boulton et al., 2014; Whittaker & Walker, 2015). Some work has focussed on long-wavelength processes using continent wide river profile inversion (G. G. Roberts et al., 2012; Czarnota et al., 2014; Paul et al., 2014; Rodríguez Tribaldos et al., 2017), while other studies have investigated smaller scale phenomena (e.g. Goren et al., 2014). This analysis quantitatively deconvolves long wavelength ‘regional’ uplift and short wavelength faulting using river profile inversion.

Geophysical and geomorphological studies suggest that Italy’s topography has been generated by active faulting and longer wavelength processes, probably associated with sub-lithospheric support (e.g. d’Agostino et al., 2001; Faure Walker et al., 2012; Faccenna et al., 2014). However, the relative contribution of these two processes to the present day topography is poorly constrained, and their rates and magnitudes of vertical motion through time remain unknown for most of the region. The aim of this paper is to investigate these processes in Calabria where geomorphological and archaeological observations, and geochronological data, help to constrain landscape evolution over a range of length and timescales (Westaway, 1993; Ferranti et al., 2006; Stanley & Bernasconi, 2012; Pirrotta et al., 2016). We use these data alongside 994 river profiles that cross all major faults in Calabria, and employ a simple stream power relationship to invert their longitudinal profiles for a spatio-temporal uplift history. We show that Calabria’s rivers record both regional uplift and changes in fault throw rate.

1.2 Geology and geomorphology of Calabria

The Cretaceous to Eocene collision of the Eurasian and African plates, which resulted in the Alpine and Pyrenean orogenies in Western Europe, caused profound changes to the landscape of the Mediterranean region. The subsequent segmentation of the Alps, accompanied by significant block rotations and magmatism (e.g. Rosenbaum et al., 2002; Savelli, 2002), created positive and negative changes in landscape elevation on geologic and historical timescales (e.g. Braga et al., 2003; Fellin et al., 2005; Ferranti et al., 2008; Scicchitano et al., 2008; Antonioli et al., 2009). However, the extent to which the present-day topography of Southern Italy records crustal stresses, plate flexure, mantle processes or climate change is poorly understood.

The geology of Calabria reveals the dramatic paleogeographic change of southwest Europe since Late Eocene–Oligocene cessation of Alpine compression. Its basement of granites, gneisses and schists (Figure 1), which were deformed during the Variscan orogeny, indicate that Calabria was positioned on the Eurasian margin prior to Alpine collision (Rossetti et al., 2001, 2004; Rosenbaum et al., 2002). Metamorphosed ophiolites in the Alpine Nappes (Figure 1) and high pressure–low temperature metamorphism imply that the region was proximal to the subduction front during the closure of Tethys (e.g. Liberi et al., 2006; Pezzino et al., 2008), with localised compression until the Pliocene (Capozzi et al., 2012).

The southern Tyrrhenian Sea has rapidly stretched since the late Miocene separation of Sardinia and Calabria, and ages of dredged oceanic crust reveal episodic oceanic

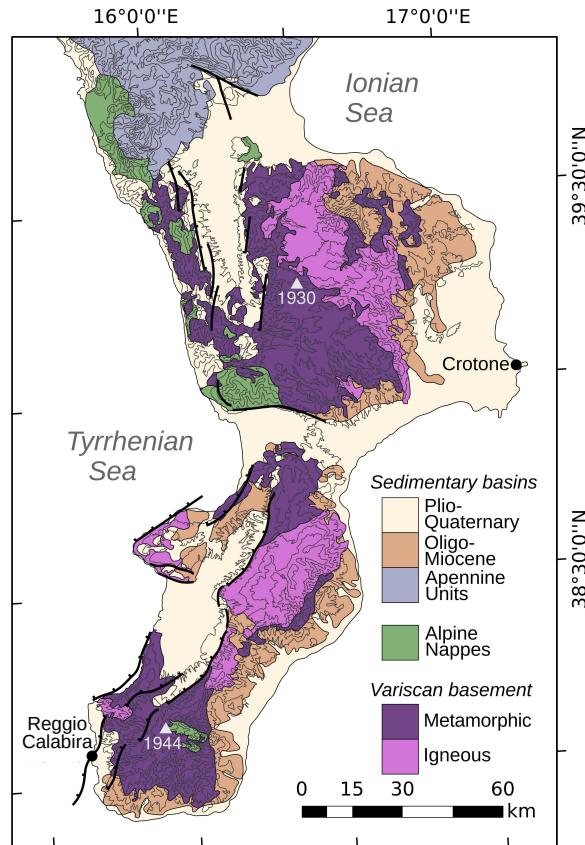


Figure 1. Simplified geological map of Calabria. Bedrock geology modified from Monaco and Tortorici (2000); Catalano et al. (2008); Minelli and Faccenna (2010); Fiannacca et al. (2015). Topographic contours at 250 m intervals, with spot elevations (grey triangles) of peaks in the Sila and Aspromonte massifs in metres. Active fault traces shown as black lines, with ticks on hanging wall.

115 spreading (Rosenbaum & Lister, 2004). Seismic tomography and deep seismicity (35 to
 116 500 km) indicate that the Tethyan oceanic plate still subducts beneath Calabria (e.g.
 117 Piromallo & Morelli, 2003; Chiarabba et al., 2005). An offshore accretionary prism is ob-
 118 served in seismic data from the Ionian Sea (Minelli & Faccenna, 2010). However, active
 119 extension is present both onshore Calabria and along its Tyrrhenian coastline, dominantly
 120 expressed as a series of NNE–SSW striking normal faults (Figure 2; e.g. Catalano et al.,
 121 2008). Numerous historical earthquakes (Figure 3b), many with devastating tsunamis,
 122 attest to the recent activity of the majority of these faults (e.g. Catalano et al., 2008;
 123 Meschis et al., 2019). This close spatial coupling of compression and extension is also
 124 observed further north in the Italian Apennines and is attributed to the roll-back of the
 125 cold subducting slab of the Tethyan oceanic plate (Malinverno & Ryan, 1986).

126 However, despite numerous observations of recent crustal extension, marine terraces
 127 and exposed tidal notches show that much of Calabria has experienced rapid Quater-
 128 nary uplift (Antonioli et al., 2009). Shear wave anisotropy measurements are consistent
 129 with mantle convection around the subducting plate (e.g. Civello & Margheriti, 2004;
 130 Baccheschi et al., 2008), which has been recently suggested as the cause of Calabria’s long
 131 wavelength uplift (Faccenna et al., 2014; Magni et al., 2014). However, little work to date
 132 has focused on isolating rates of regional uplift from dynamic mantle processes.

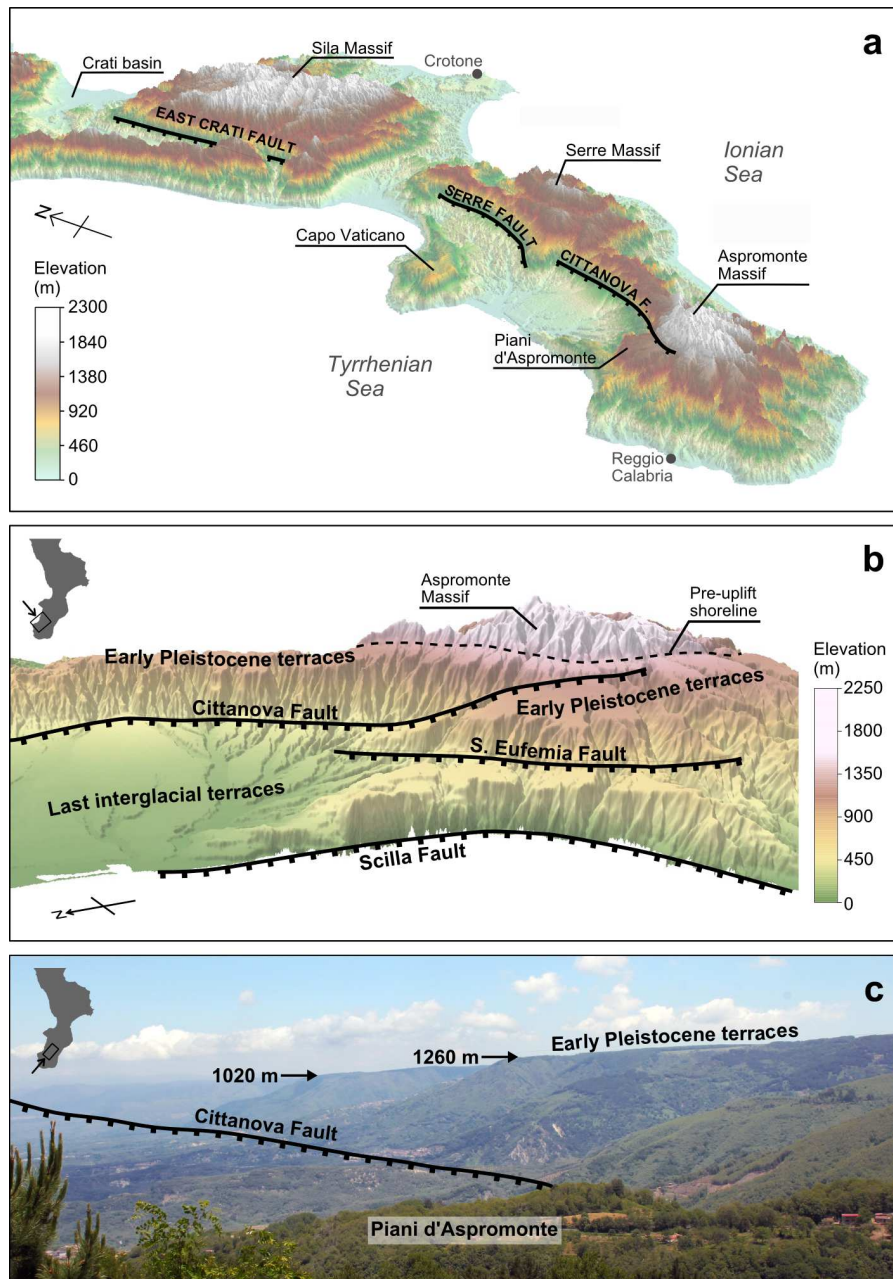


Figure 2. Geomorphologic expression of active normal faults and marine terraces in Calabria. (a) Perspective view of SRTM DEM with 2× vertical exaggeration. Selected geomorphic features and major faults labelled. (b) SRTM DEM with 1.75× vertical exaggeration, focussed on Aspromonte region. Visual extent and viewing direction shown by box and arrow on inset map. (c) Photograph of the Cittanova fault, facing north. Arrows indicate locations of footwall crests.

133

1.2.1 Geomorphic observations of Quaternary uplift

134

135

136

137

Early Pleistocene marine terraces reach heights of 1.3 km above sea level in the Aspromonte region of southern Calabria (Figure 2). These marine terraces, the oldest in the region and the only terraces found in the footwalls of the major faults, are poorly dated to 0.58 to 1.8 Ma (e.g. Tortorici et al., 1995; Catalano et al., 2008; Roda-Boluda

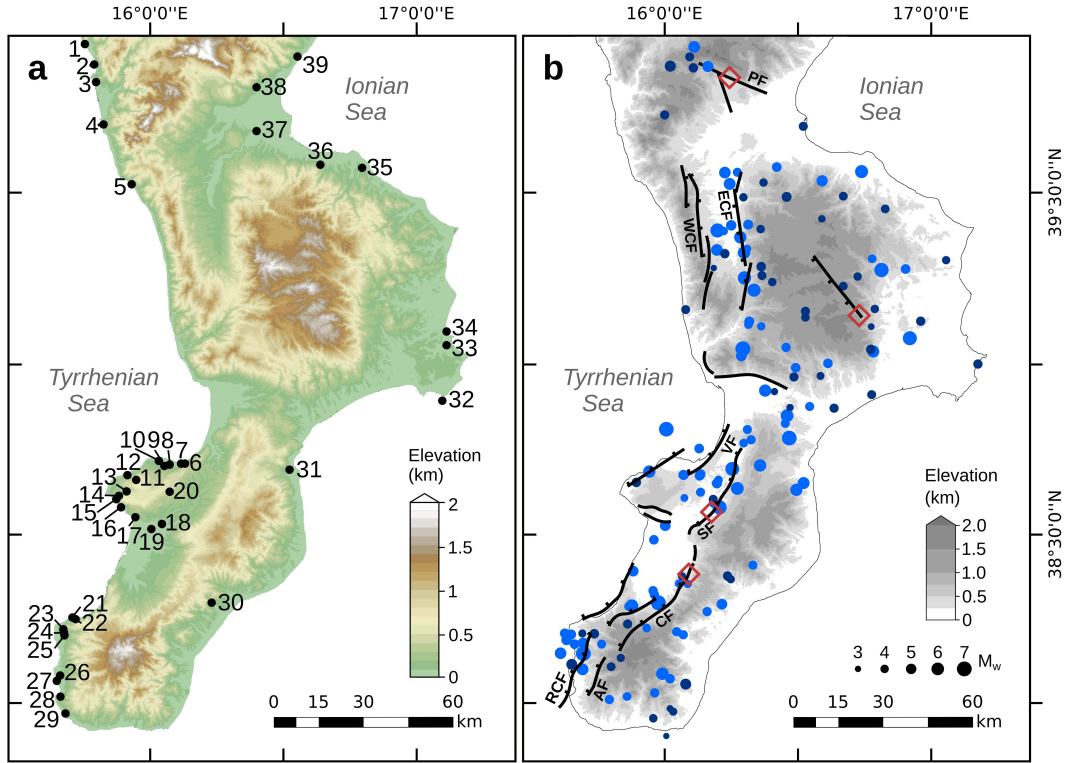


Figure 3. Calabria’s marine terraces and historical / paleoseismicity. (a) Locations of Pleistocene–Recent marine terraces reported in literature (for reference to ID numbers see Table 1). (b) Earthquake epicentres from the INGV 2015 seismic catalogue. Only earthquakes reported at >2 locations in the catalogue are included in this Figure to ensure robust triangulation of earthquake epicentres. Pre- 1970: light blue circles. Post- 1970: dark blue circles. Red diamonds: dated trenching sites (Galli et al., 2008). PF: Pollino fault; WCF: West Crati fault; ECF: East Crati Fault; VF: Vibo fault; SF: Serre fault; CF: Cittanova fault; AF: Armo fault; RCF: Reggio Calabria fault.

138 & Whittaker, 2017). However, a probable age is the Sicilian Stage (0.8–1.2 Ma), based
 139 primarily on the first appearance of ‘boreal guests’ including *Artica islandica* and *Hya-*
 140 *linea balthica* (e.g. Miyauchi et al., 1994). The oldest terraces are easily identified by their
 141 well-preserved wave cut platforms flanking the higher relief massifs (Miyauchi et al., 1994;
 142 Roda-Boluda & Whittaker, 2017). The widespread nature of these marine terraces demon-
 143 strate that the majority of Calabria’s topography has probably developed since the Si-
 144 cilian Stage and indicate that much of the region was below sea level prior to this time.
 145 The massifs of weathered Paleozoic crystalline basement (with peaks \approx 1.8 km above
 146 sea level) are interpreted as an archipelago of small islands, which were sub-aerially ex-
 147 posed prior to the initiation of uplift (e.g. Westaway, 1993).

Last-interglacial (MIS 5e) tidal notches and marine terraces are identified along Cal-
 abria’s coastline due to the presence of *Strombus bubonius* and other warm-water ‘Sene-
 galese’ fauna, U-Th coral ages and amminoacid racimization correlation (Figures 2b and
 3a; Table 1). Tectonic uplift rates can be calculated from marine terraces using

$$U = \frac{H_t - S_H}{\Delta t} \quad (1)$$

148 where U is uplift rate, H_t is the observed elevation of the marine terrace, S_H is the re-
 149 lative sea level at the time of terrace formation (where positive values of S_H denote sea

150 levels higher than present) and Δt is the time since terrace formation (e.g. Ferranti et
 151 al., 2006). The heights of last interglacial terraces are highly variable across Calabria,
 152 with the highest uplift rates ($>2.5 \text{ mm yr}^{-1}$ for the last 124 ka) observed in footwalls of
 153 faults on the Capo Vaticano peninsula (Bianca et al., 2011). Lower uplift rates (0.47 to
 154 0.89 mm yr^{-1} for the last 124 ka) exist in the adjacent, and relatively subsiding, hang-
 155 ing wall of the Cittanova fault (Table 1 and Figure 3). Terrace heights in the Crotone
 156 Basin, $>50 \text{ km}$ from major active faults, are indicative of consistently low uplift rates
 157 ($<1 \text{ mm yr}^{-1}$; Table 1: ID 32 to 34). Holocene uplift rates show similar spatial variabil-
 158 ity to the Late Pleistocene rates, yet may imply a temporal increase in uplift rate near
 159 the Messina Strait (Antonioli et al., 2006).

160 However, absolute ages of older terraces are scarce across much of Calabria. Op-
 161 tically Stimulated Luminescence dating of 125–380 m elevation marine terraces on the
 162 Capo Vaticano peninsula yielded ages of $184 \pm 20 \text{ ka}$ to $214 \pm 25 \text{ ka}$, corresponding to
 163 highstands within MIS 7 (Figure 3; Table 1 Bianca et al., 2011). The presence of higher,
 164 though currently undated, terraces on Capo Vaticano mean that these observations are
 165 consistent with uplift initiating prior to 200 ka (Bianca et al., 2011). Isolated marine ter-
 166 races mapped in northern Calabria (e.g. Isola di Dino) do not have robust absolute age
 167 constraints (see Table 1; Figure 3: ID 1–5, 38–40), and, as such, different ages have been
 168 attributed to the same terrace (Carobene & Dai Pra, 1990; Westaway, 1993). In general,
 169 the superposition of normal faulting and regional uplift complicates terrace correlation
 170 across Calabria, and the uneven distribution of uplift constraints can make it difficult
 171 to fully quantify—and make comparisons of—fault growth or regional uplift.

172 Several local studies show that Calabria’s rivers have transient longitudinal pro-
 173 files containing at least one knickpoint (e.g. Pirrotta et al., 2016; Roda-Boluda & Whit-
 174 taker, 2017; Robustelli, 2019), which also suggests that uplift has varied both spatially
 175 and temporally across the region. Catchment averaged erosion rates derived from cos-
 176 mogenic nuclide concentrations are similarly variable. Erosion rates are generally low at
 177 high elevations within the massifs or above fluvial knickpoints ($\sim 0.1 \text{ mm yr}^{-1}$), and are
 178 higher (up to 1.6 mm yr^{-1}) upstream of active faults or in small catchments close to the
 179 coast below a major knickpoint (Cyr et al., 2010; Olivetti et al., 2012; Roda-Boluda et
 180 al., 2019).

181 **1.2.2 Active faults in Calabria**

182 Over 130 moderate to large magnitude earthquakes ($3.1 \leq M \leq 7.1$) with well-
 183 constrained epicentres have been documented throughout Calabria in the last ca. 1000 yr
 184 (Rovida et al., 2016). The wide spatial distribution of their epicentres indicates the pres-
 185 ence of many active faults (Figure 3b). Radiocarbon dating of trenched normal faults
 186 and damage to archaeological sites provides evidence for Holocene activity of some struc-
 187 tures (Galli & Bosi, 2002; Galli et al., 2007; Cinti et al., 2015). Many of Calabria’s faults
 188 have a clear geomorphic expression that can be mapped from digital elevation models
 189 (Figure 2), and the large fault scarps imply that seismicity originated during the Pleis-
 190 tocene (e.g. Monaco & Tortorici, 2000; Catalano et al., 2008). Major faults pertinent
 191 to this study will be discussed in detail below.

192 The NW dipping NE–SW striking Cittanova fault lies entirely onshore, and has the
 193 longest fault trace ($\sim 42 \text{ km}$) in Calabria (Catalano et al., 2008). With fault segments
 194 of $\sim 10 \text{ km}$, the Cittanova fault probably reached its current size though the interaction
 195 of a series of *en echelon* normal faults, whose connecting relay ramps have since been
 196 breached (e.g. Fossen & Rotevatn, 2016). This model of fault growth is supported by
 197 the presence of knickpoints along tributaries of the Petrace river, which have been in-
 198 terpreted as the geomorphic expression of increases in throw rate (Pirrotta et al., 2016;
 199 Roda-Boluda & Whittaker, 2017). Further north, the Serre fault has a similar *en ech-*
 200 *elon* morphology and a length of 35 km (e.g. Galli et al., 2008). Along with the Armo
 201 fault in the south, they form a linked fault array (Roda-Boluda & Whittaker, 2017), which

was probably responsible for the $6.74 \leq M \leq 7.1$ earthquake sequence in 1783 (Galli & Bosi, 2002).

Published estimates of average throw rate since the onset of faulting for the Cittanova fault lie in the range 0.4 mm yr^{-1} to $1.4^{+0.7}_{-0.5} \text{ mm yr}^{-1}$ (Westaway, 1993; Roda-Boluda & Whittaker, 2017). Throw rate estimates are similar for the Serre fault, ranging from $0.6\text{--}0.7 \text{ mm yr}^{-1}$ (Catalano et al., 2008) to $0.8^{+0.3}_{-0.2} \text{ mm yr}^{-1}$ (Roda-Boluda & Whittaker, 2017). These calculations are based upon an assumed age of the oldest off-set marine terrace (Section 1.2.1).

The smaller Scilla, Santa Eufemia and Reggio Calabria faults lie close to the Messina Strait in the south west of the region, creating a half-graben that is clearly expressed in the topography of the Aspromonte area (Figure 2b). Synchronous terrace correlation shows that the Vibo fault, on the Tyrrhenian coast of central Calabria, has experienced a throw rate of $\sim 1 \text{ mm yr}^{-1}$ since 340 ka (G. P. Roberts et al., 2013). In the north of Calabria lies the Crati basin, a graben bounded by the West and East Crati faults. Both faults strike approximately N–S and their traces can be mapped at the surface for $\sim 50 \text{ km}$ (Figures 1 and 2). Offset horizons in reflection seismic data indicate an average throw rate for the East Crati fault of $\geq 0.9 \text{ mm yr}^{-1}$ since 0.7 Ma (Spina et al., 2011). This estimate agrees with an average throw rate of $1.3^{+0.7}_{-0.5} \text{ mm yr}^{-1}$ calculated using geomorphic measurements (Roda-Boluda & Whittaker, 2017). Cosmogenic nuclide catchment averaged erosion rates from the footwalls of the Serre-Cittanova-Armo fault array vary along strike, and some erosion rates equal—within error—the throw rates estimated by geomorphic and geologic analyses (Roda-Boluda et al., 2019). On average, however, catchment averaged erosion rates are a factor of two smaller than uplift rates; this discrepancy probably arises because catchments are only partially incised by rivers and may have experienced different amounts of landsliding (Roda-Boluda et al., 2019). These correlations suggest that rates of surface processes can be used to investigate rates of active faulting.

While the geologic throw and time-averaged displacement rates for the largest faults have been constrained since fault initiation, changes in throw rate have proved more difficult to analyse because paleoseismicity can only analyse relatively short timescales compared to geological or geomorphological data (e.g. Galli et al., 2007; Roda-Boluda & Whittaker, 2017). In this paper, we investigate whether fluvial inversion can help to further constrain the temporal history of active faulting in Calabria. In particular, we will focus on the East Crati, Serre and Cittanova faults.

2 Methods

2.1 Longitudinal profile generation

To extract a fluvial drainage network across Calabria, Esri’s steepest descent flow routing algorithms (Flow Direction and Flow Length), were applied to the SRTM 1 arc second ($\approx 30 \text{ m}$ spatial resolution) digital elevation model (Tarboton, 1997; Stucky de Quay et al., 2017). An upstream drainage area of 0.32 km^2 is assumed to approximate the threshold for fluvial incision, and cells with this upstream area were systematically sampled to provide the heads of rivers for this study. This technique results in good spatial coverage of the fluvial network and does not bias against rivers of a particular length or stream order assuming that more rivers are extracted from larger catchments. The cumulative number of cells that flow into each catchment (Flow Accumulation) was multiplied by cell resolution ($30 \times 30 \text{ m}$) to calculate upstream area, A . The morphology of the extracted fluvial drainage network was verified using a combination of aerial photography, published maps (e.g. Pirrotta et al., 2016) and field surveying. The result of longitudinal profile extraction is shown in Figure 5a.

Two versions of this river inventory were used for fluvial inverse modelling: The first comprised a network across the whole of Calabria, as presented in Figure 5. For the second inventory, we removed all rivers draining the large Crati Basin (Figure 5), where

254 present observations of alluviated channels close to the river mouth suggest that a stream
 255 power erosion model may be less appropriate. The results of the inverse model from the
 256 second river inventory are presented in the Supplementary Information; the differences
 257 between the two models are quantified and discussed therein, and in section 3.1.

258 2.2 Stream power erosion models

Field observations show that many of Calabria’s large rivers flow over bedrock with sparse alluvial cover, particularly in the vicinity of the normal faults in the west of the region (e.g. Roda-Boluda & Whittaker, 2017), which suggests that fluvial erosion can be approximated using a detachment-limited model (e.g. Howard, 1994). Erosion rate in a stream power model is parametrised as a function of channel slope, width and discharge (Howard, 1994). Upstream area, A —measured from digital elevation models—is a useful surrogate for discharge and channel width, which are difficult to quantify over geological timescales. Assuming the rate of elevation change, $\partial z/\partial t$, is the sum of uplift rate, U , and erosion rate, E , a simple version of the stream power model can be expressed as

$$\frac{\partial z}{\partial t} = U(x, t) + E(x, t), \quad \text{where} \quad E = -kA^m \left(\frac{\partial z}{\partial x} \right)^n, \quad (2)$$

259 where k is a constant of proportionality often linked to erodibility of the bedrock
 260 (e.g. Whipple, 2004; Lague, 2014), and $\partial z/\partial x$ is the longitudinal channel slope. Expo-
 261 nents m and n are positive and are usually empirically evaluated. The exponent, n , de-
 262 termines the dependency of erosion rate on channel gradient, and in theory controls the
 263 rate of landscape response to perturbation. If n is not equal to 1, the record of tectonic
 264 signals can be lost through the formation of shocks and discontinuities (e.g. Pritchard
 265 et al., 2009; Royden & Perron, 2013; Lague, 2014; Harel et al., 2016). While theoreti-
 266 cal considerations may predict that $n > 1$ —if erosion is controlled by thresholds asso-
 267 ciated with stochastic weather events for instance (e.g. Lague, 2014)—field and theoret-
 268 ical studies of rivers crossing active faults in the central Apennines and southern Italy,
 269 where the magnitudes and distributions of unit stream powers scale predictably with struc-
 270 tural and geomorphic measures of footwall uplift, suggest that $n \approx 1$ is reasonable for
 271 this area (e.g. Whittaker et al., 2008; Attal et al., 2011; Whittaker & Boulton, 2012; Roda-
 272 Boluda et al., 2018). Similarly, joint-inversion of drainage networks is also consistent with
 273 $n \approx 1$ in a number of settings (e.g. Paul et al., 2014; Rudge et al., 2015; McNab et al.,
 274 2018). If $n \approx 1$, there is a simple, physical relationship between erosion process and chan-
 275 nel slope (e.g. Whipple & Tucker, 1999), and the stream power model can be solved us-
 276 ing a computationally efficient linearised inversion approach (Goren et al., 2014; Rudge
 277 et al., 2015; Glotzbach, 2015). Consequently, we proceed with $n = 1$, though we acknowl-
 278 edge that the value of this exponent remains contentious, and we therefore return to this
 279 assumption in the discussion.

280 An increase in uplift rate can produce changes in the slope, $\partial z/\partial x$, of longitudi-
 281 nal river profiles known as knickpoints and knickzones. However, an important consid-
 282 eration when interpreting the shape of longitudinal river profiles is the contribution from
 283 changes in bedrock competence and discharge. Tensile and compressive rock strength
 284 is often used a proxy for bedrock erodibility as a function of lithology (e.g. Sklar & Di-
 285 etrich, 1998; G. G. Roberts & White, 2010; Zondervan et al., 2020). In Calabria, the com-
 286 pressive strength of bedrock along river channels has been recently measured using a Schmidt
 287 hammer by Roda-Boluda et al. (2018). These authors found that median Schmidt ham-
 288 mer rebound values were generally low, < 35 , suggesting that bedrock is weak across a
 289 range of lithologies. These observations indicate that lithology probably does not deter-
 290 mine the position of Calabria’s knickpoints, therefore we may make the simplifying as-
 291 sumption that k is a constant. In addition, if knickpoints are generated by differences
 292 in rock strength, we may expect knickpoints to systematically correlate with the posi-
 293 tion of lithologic transitions (e.g. Wobus et al., 2006). Therefore, we will compare the

294 location of channel slope discontinuities with mapped bedrock geology to evaluate the
 295 assumption that changes in lithology do not control the shape of longitudinal profiles.

296 It is possible for fluvial drainage networks to be modified during glacial periods.
 297 A few glacial deposits were mapped on the highest peaks in the Pollino range, on Mt Sila,
 298 and in northeastern Calabria (Palmentola et al., 1990). However, since terminal moraines
 299 are found >1400 m above sea level, and are distributed in an area that lies upstream of
 300 the threshold for fluvial incision, we conclude that Pleistocene glaciation had a negli-
 301 gible effect on Calabria’s fluvial drainage network (Palmentola et al., 1990). Mean annual
 302 precipitation measured across Calabria indicates that present-day coupling between el-
 303 evation and precipitation is very weak (D’Arcy & Whittaker, 2014). Moreover, as Cal-
 304 abria has been rapidly uplifted from sea level during the last ~ 1 Ma it is unlikely that
 305 Pleistocene orographic precipitation was more significant than at present (section 1.2.1).
 306 Paleoclimate reconstructions suggest rainfall in Southern Europe did not greatly differ
 307 between glacial and interglacial periods (Braconnot et al., 2007). Therefore, climatic changes
 308 are unlikely to drive long period differences in fluvial erosion rate across Calabria, and
 309 we will assume that discharge, which controls erosion rate in the stream power model
 310 through upstream area, A , does not vary through time to avoid unconstrained model in-
 311 puts.

312 The major drainage divide passes through the high relief massifs in central Cal-
 313 abria (Figures 2 and 5), implying that large scale drainage reorganisation has not oc-
 314 curred since uplift initiated at ~ 1 Ma. Consequently, we suggest that the majority of
 315 observed knickpoints are unlikely to have been generated by drainage divide migration
 316 (cf. Willett et al., 2014). Instead, the high number of knickpoints and knickzones across
 317 the region, many of which are far from the major drainage divide or upstream of active
 318 faults, suggest that fluvial channels are responding to rock uplift at a variety of spatial
 319 and temporal scales.

320 2.3 Fluvial inverse modeling

321 We used the joint spatial and temporal fluvial inversion model of Rudge et al. (2015)
 322 to predict the cumulative uplift of Calabria since the exposure of the oldest marine ter-
 323 race at 0.8–1.2 Ma (section 1.2.1). The advantages of using this type of inverse model
 324 include the ability to simultaneously analyse large numbers of river profiles and to cal-
 325 culate uplift rates without the need to pick or classify knickpoints. Moreover, the details
 326 of fault location, activity and linkage history do not need to be established in advance.

327 The inverse model solves for the spatial distribution of uplift rate on a regular tri-
 328 angular grid that was generated from evenly spaced vertices 10 km apart. A 10 km ver-
 329 tex spacing ensures that at least part of a river exists within the vast majority of grid
 330 cells, so the inverse model can resolve recent uplift rates for most of Calabria. This ver-
 331 tex spacing is generally less than the fault separation (Figure 3), and is much smaller
 332 than the area believed to be influenced by regional uplift (Section 1.2), therefore our in-
 333 verse model should be able to capture uplift caused by both the faulting and regional
 334 uplift processes that are known to modify Calabria’s landscape. By modeling uplift on
 335 an arbitrary grid (i.e. without specifying fault position *a priori*) we can investigate if
 336 the inverse model replicates expected geologic behaviour such as divergence in uplift rate
 337 across a mapped fault. Spatial variation in uplift rate was linearly interpolated between
 338 vertices using barycentric co-ordinates. Predicted uplift rate was permitted to vary at
 339 30 evenly distributed time steps.

340 From Equation 2, the time, τ , for a knickpoint to travel between longitudinal dis-
 341 tances x_0 and x_1 can be written as

$$\tau = \int_{x_0}^{x_1} \frac{1}{kA(x)^m} dx, \quad (3)$$

342 where k is a proxy for bedrock erodibility and $A(x)^m$ defines how erosion depends
 343 on upstream catchment area, A . Therefore, the predicted elevation, z_t , of a river chan-
 344 nel as a function of distance, x , can be calculated using

$$z_t = \int_0^\tau U(x(t), t) dt, \quad (4)$$

345 where $U(x(t), t)$ is uplift rate as a function of space and time, which is integrated
 346 along the time-longitudinal distance path of Equation 3 to derive elevation. For the meth-
 347 ods employed in this analysis, Equations 3 and 4 were evaluated using the trapezium rule
 348 in order to find the uplift history that produced the observed longitudinal profiles (Rudge
 349 et al., 2015). Equations 3 and 4 show that the stream power incision model (Equation 2)
 350 can be linearised such that, $\mathbf{z} = \mathbf{M}\mathbf{U}$, where elevation and uplift values are given by the
 351 vectors \mathbf{z} and \mathbf{U} , respectively. This problem tends to be under-determined (i.e. there are
 352 more possible uplift models than can be constrained by fluvial profile observations alone),
 353 so the inversion model minimises

$$|\mathbf{M}\mathbf{U} - \mathbf{z}|^2 + \lambda_s^2 \int_s \int_{t=0}^{t_{max}} |\nabla U|^2 dt ds \quad \text{subject to: } U \geq 0, \quad (5)$$

354 where the value of λ_s determines damping in space, s . Time at the present-day is de-
 355 noted by $t = 0$, and t_{max} is the maximum possible τ for all rivers assuming that a knick-
 356 point can travel from the river mouth to the river head (Rudge et al., 2015). Note that
 357 knickpoints can be generated at any position along the river profile using this inverse scheme.
 358 Equation 5 was minimised using the non-negative least squares Broyden-Fletcher-Goldfarb-
 359 Shanno algorithm of Zhu et al. (1997). The initial uplift rate guess for least-squares min-
 360 imisation is $U = 0$ at all nodes in space and time. A positive uplift rate as a function
 361 of space and time was incorporated at subsequent iterations if required to produce a bet-
 362 ter fit between observed and predicted longitudinal profiles. We assume that Equation 5
 363 is minimised when the difference between consecutive iterations is $<10^{-6}$. The uplift rate,
 364 as a function of space and time, that minimises Equation 5 is henceforth known as the
 365 best-fitting uplift model.

366 We followed Parker (1977)'s protocol to seek the smoothest model with the low-
 367 est root-mean-squared (rms) misfit, which we will evaluate using independent geologic
 368 constraints. In general, inverse models that are highly damped (e.g. $\lambda_s \gg 1$) produce
 369 smooth uplift with large rms misfit. A very smooth model (large 'model norm') might
 370 not incorporate short wavelength changes in uplift related to normal faulting, and as such
 371 would be unsuitable for Calabria. However, models with little damping (e.g. $\lambda_s \ll 1$)
 372 can over-fit the data and may be fitting noise (e.g. Parker, 1977). We performed a sys-
 373 tematic test of model damping, in which λ_s was varied between 10^{-3} and 10^3 to find an
 374 appropriate value of λ_s for this model, and we subsequently evaluate the influence of spa-
 375 tial damping on apparent fault timing (see section 3.2 and Supplementary information).

376 We calculated the root-mean-squared (rms) misfit to evaluate the extent to which
 377 river profiles predicted by the best fitting uplift model correspond to the observed lon-
 378 gitudinal profiles. The rms misfit, H , was calculated using

$$H = \sqrt{\frac{1}{N} \sum_{i=1}^N \left(\frac{z_{i,o} - z_{i,t}}{\sigma_i} \right)^2}, \quad (6)$$

379 where N is the total number of elevation measurements, σ is the error in the observed
 380 data, and z_o and z_t are elevations of observed and predicted longitudinal river profiles,
 381 respectively. The absolute vertical error of SRTM 1 arc second data in high relief regions
 382 is ≈ 16 m (e.g. Mukul et al., 2017), so we set $\sigma = 16$ m.

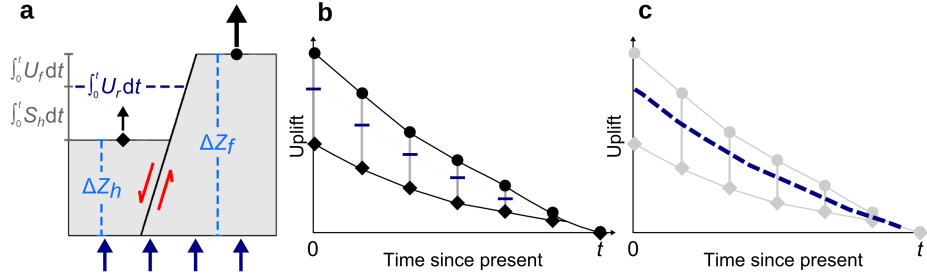


Figure 4. Graphical representation of procedure to deconvolve regional uplift from results of fluvial inverse modeling. (a) Fault cross section showing the relative observed uplift, ΔZ_f , in fault footwall (circles) and ΔZ_h in fault hanging wall (diamonds) for constant regional uplift (blue arrows). U_f and S_h indicate magnitudes of footwall uplift rate and hanging wall subsidence rate, respectively. Dashed dark blue line represents the magnitude of regional uplift, U_r , between time t and the present day $t = 0$. (b) Uplift as a function time in the footwall and hanging wall (circles and diamonds respectively) with calculated regional uplift denoted by blue dashes. (c) As (b) but with regional uplift linearly interpolated between time t and the present day.

383 Inverse approaches can systematically test how the exponent of upstream area, m ,
 384 affects rms misfit and calculated uplift. Most published values of m lie between 0.2–1.0,
 385 and $m = 0.5$ is commonly reported for fluvial settings (e.g. Howard & Kerby, 1983; Bishop
 386 et al., 2005; Loget & Van Den Driessche, 2009). Therefore, we repeated the inversion pro-
 387 cedure with values of m between 0.1 and 1.0 and assumed that suitable average m val-
 388 ues will produce low rms misfits. We also used the inversion modelling to evaluate the
 389 average value of bedrock erodibility, k , for Calabria given the time constraints on the age
 390 of the upper terrace (approximately 0.8–1.2 Ma, see section 1.2.1).

391 To test the accuracy of our uplift model, we compared uplift rates relative to present
 392 day sea level calculated from marine terrace heights to those predicted by inverse mod-
 393 elling since interglacials MIS 5 and MIS 7. This comparison was restricted to marine ter-
 394 races with absolute dating constraints, though still incorporates localities across the re-
 395 gion, including the minimum and maximum uplift rates since the last interglacial high-
 396 stand. For terraces >2 km away from a model vertex, the cumulative uplift from the maps
 397 of Figure 9 was linearly interpolated so the terrace uplift rate and inverse model uplift
 398 rate were compared at the same spatial location. As geologic and geomorphic evidence
 399 suggests most of Calabria was a submarine environment prior to early Pleistocene time
 400 (section 1.2.1), and to facilitate comparison between the uplift rates predicted by fluvial
 401 inversion and marine terrace elevations, we have opted to use sea level as the most ap-
 402 propriate river base level in this study.

403 2.4 Deconvolution of normal faulting and regional uplift

404 Calabria is experiencing simultaneous regional uplift and extensional faulting, which
 405 has resulted in some fault hanging walls being uplifted relative to sea level (Figure 2; Fig-
 406 ure 4a). To deconvolve regional uplift and normal faulting, we first extracted cumula-
 407 tive uplift from the best-fitting inverse model at locations in the footwalls and hanging
 408 walls of mapped faults to estimate long-term throw rates. We subsequently used ratios
 409 of footwall uplift to hanging wall subsidence to estimate regional uplift through time
 410 at the same location. If the oldest terrace (Sicilian Stage, 0.8–1.2 Ma) can be correlated
 411 across the tip of a fault, being observed in both the footwall and proximal hanging wall,
 412 we can calculate regional uplift using

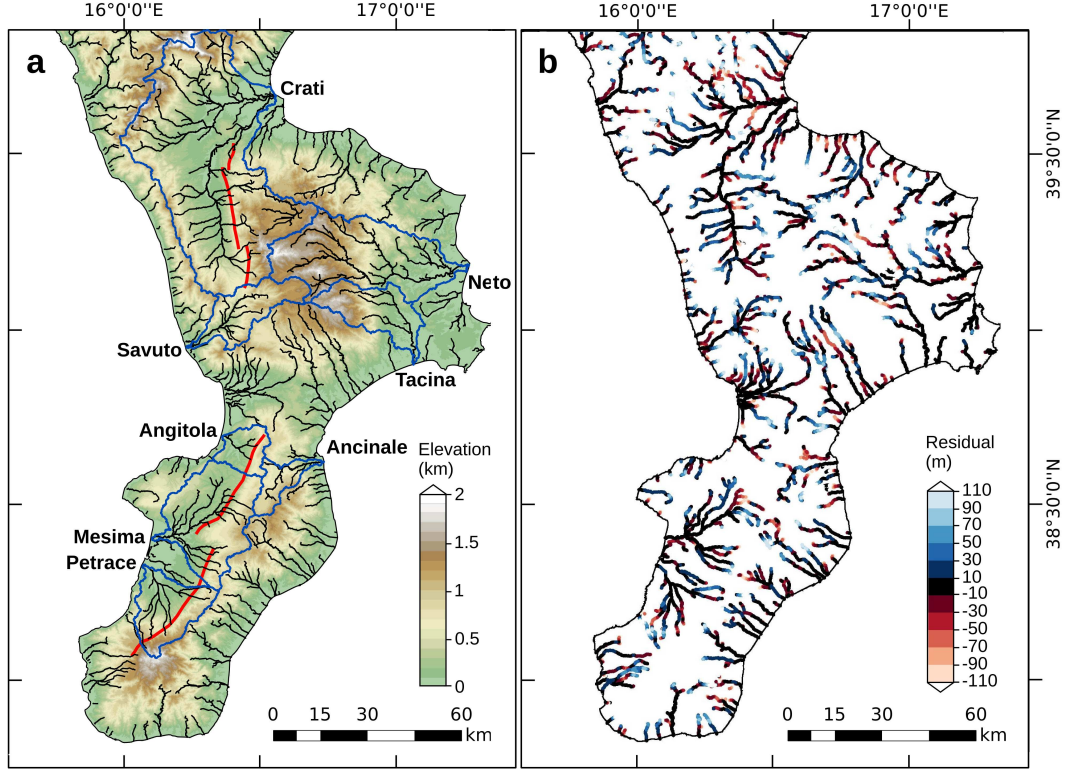


Figure 5. Results of drainage extraction and longitudinal profile modeling. (a) Plan view of extracted river profiles overlain on SRTM DEM. Drainage divides of major river basins as blue lines. East Crati, Serre and Cittanova fault traces denoted by red lines (see Figure 2). (b) Elevation residuals between observed and calculated river longitudinal profiles.

$$\Delta Z_h = \int_t^T U_r dt - \int_t^T S_h dt, \quad (7)$$

$$\Delta Z_f = \int_t^T U_r dt + \int_t^T U_f dt, \quad (8)$$

$$\int_t^T S_h dt = \alpha \int_t^T U_f dt, \quad (9)$$

where ΔZ_h and ΔZ_f are changes in the elevation of hanging wall and footwall, respectively. U_r , S_h and U_f are the rates of regional uplift, hanging wall subsidence and footwall uplift between times t and T (Figure 4a). α is the ratio of hanging wall subsidence to footwall uplift. Substituting Equations 8 and 9 into Equation 7, and rearranging, yields cumulative regional uplift, such that

$$\int_t^T U_r dt = \frac{\Delta Z_h + \alpha \Delta Z_f}{(\alpha + 1)}. \quad (10)$$

413

Equation 10 can be applied to the inverse model output at every time step to estimate regional uplift through time (Figure 4b,c).

414

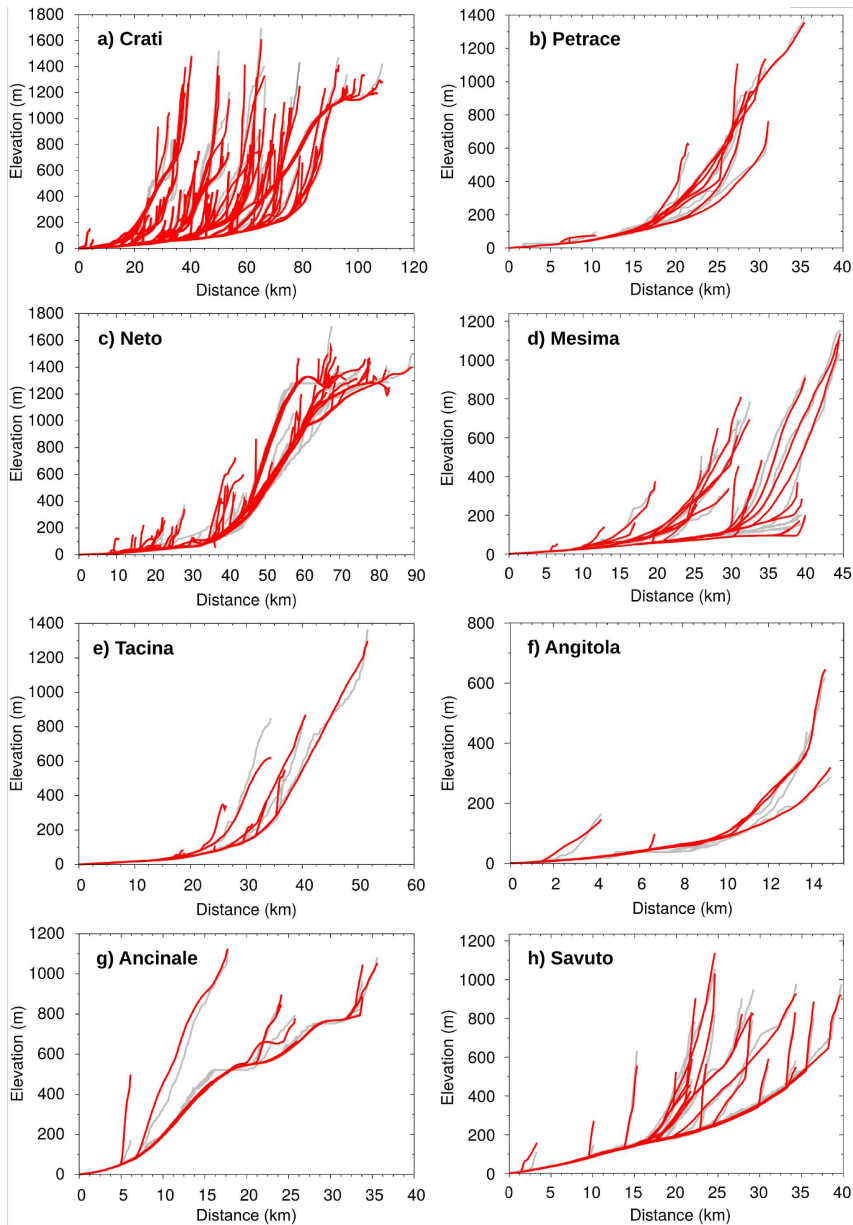


Figure 6. Longitudinal profiles from SRTM data and fluvial inverse modelling. (a–h) Longitudinal profiles extracted from SRTM DEM for the eight catchments highlighted in Figure 5 (plotted as gray lines) and theoretical river profiles (red lines) calculated using uplift history shown in Figure 9.

415

3 Results and discussion

416

417

418

419

420

421

422

The majority of Calabria’s rivers contain at least one knickpoint or knickzone (Figures 6 and 7). Knickpoints reside at $\approx 100\text{--}1200$ m above sea level and do not tend to coincide with changes in bedrock outcrop or the position of normal faults (Figure 7). Nevertheless, many knickpoints are observed upstream of normal faults (Figure 7a,b,d,f). These observations suggest that Calabria’s rivers record uplift that varies in both space and time, in agreement with existing studies at a smaller scale (Roda-Boluda & Whittaker, 2017).

423 A value of $\lambda_s \approx 1$ produces a combination of suitable model roughness (a small
 424 ‘model norm’) and low rms misfit for Calabria (Figure 8a), which is similar to the op-
 425 timal value used in many previous studies (e.g. Rudge et al., 2015; G. G. Roberts et al.,
 426 2018; Conway-Jones et al., 2019). Therefore, our uplift analysis will initially consider
 427 inverse models with $\lambda_s = 1$. We will subsequently test the influence of the λ_s value on
 428 the apparent fault timing and throw rates inferred from the fluvial inverse model. For
 429 $\lambda_s = 1$, the inverse model fits the data poorly if $m \lesssim 0.3$ or $m \gtrsim 0.75$, which is con-
 430 sistent with previous inversion studies (Figure 8b; e.g. G. G. Roberts et al., 2012). To
 431 further constrain the value of m , we compared the elevation of Capo Vaticano’s high-
 432 est terrace, with a mean elevation of 550 m above sea level, to the cumulative uplift cal-
 433 culated from three vertices that intersect the terrace (Figure 8c). We aimed to produce
 434 models with similar mean elevation to this terrace that also generated theoretical river
 435 profiles with a low rms misfit (Figure 8b and c). These results suggest that $m = 0.65$
 436 is appropriate for fluvial erosion in Calabria.

437 The rms misfit, H , is 1.63 for the best fitting uplift model when $m = 0.65$ and $\lambda_s = 1.0$.
 438 Although the H value is close to unity, implying that—on average—the inverse model
 439 almost replicates the observed longitudinal profiles within error, some rivers have bet-
 440 ter fits than others. Therefore, we calculated the difference between the observed chan-
 441 nel elevation and the channel elevation predicted by the inverse model (the ‘elevation resid-
 442 ual’, $z_i^o - z_i^f$) as a function of downstream distance for every river (Figure 5b). The el-
 443 evation residuals are normally distributed with a mean of -0.04 m, which suggests that
 444 the majority of channel elevations are replicated accurately by the inverse model and el-
 445 evation is not systematically under- or over-predicted. The standard deviation of the el-
 446 evation residuals is 26 m, which is the same order of magnitude as the absolute verti-
 447 cal error of the SRTM dataset. The largest elevation residuals occur in steep headwa-
 448 ters and across lakes (Figures 5 & 6). In general, high residuals are principally a func-
 449 tion of model damping, though the accuracy of the SRTM data is also likely to decrease
 450 significantly in the steep and narrow topography of Calabria’s headwaters (Miliaresis &
 451 Paraschou, 2005; Mukul et al., 2017). Figures 6 show the best-fitting longitudinal pro-
 452 files of the eight catchments highlighted in Figure 5a.

453 Cumulative uplift for the last twenty model time steps is shown in Figure 9a, and
 454 uplift rates at each of these time steps are illustrated in Figure 10. We intend to use our
 455 fluvial inversion model to analyse the uplift that produced the Pleistocene–Recent ma-
 456 rine terraces, therefore the first time step at which the inversion produces uplift is des-
 457 ignated an age of 0.8–1.2 Ma (based upon the age of the oldest marine terrace, see sec-
 458 tion 1.2). The age range on the maps in Figures 9a and 10 encompasses the uncertainty
 459 in the oldest terrace age at all subsequent time steps. An initial uplift time of 0.8–1.2 Ma
 460 corresponds to an average bedrock erodibility $k = 0.82\text{--}1.22 \text{ m}^{(1-2m)} \text{ Myr}^{-1}$ (note that
 461 an older landscape age would linearly decrease k , and a younger landscape age would
 462 linearly increase k because bedrock erodibility is directly proportional to erosion rate ac-
 463 cording to Equation 2).

464 An uplift event that occurred at a place and time when ‘model coverage’ was > 0
 465 should still be recorded on river profiles today (Figure 9b). Model coverage, whose value
 466 depends upon the number of channel measurements between mesh vertices as well as stream
 467 power parameters k and m , decreases at earlier model time steps (Figure 9b). This de-
 468 crease in model coverage occurs because the wave of fluvial erosion continually migrates
 469 upstream through time according to the stream power equation. Some knickpoints may
 470 have reached the river head between the start of uplift and the present day, so uplift events
 471 that produced those knickpoints would not be resolved by the inverse model. Nonethe-
 472 less, model coverage is > 0 over most of Calabria during the last ~ 700 ka, which implies
 473 that an uplift history can be produced for most of the region at the majority of time steps.

474 Predicted cumulative uplift from inverse modelling first exceeds 1 km magnitude
 475 in the north of Calabria (at ~ 300 ka), then in the Aspromonte region. Uplift of the Serre
 476 and Sila Massifs is calculated to occur from 550 ka in the model with initial uplift at 1 Ma,
 477 with ≈ 1 km of uplift prior to 100 ka in the Serre area. A similar pattern of surface up-

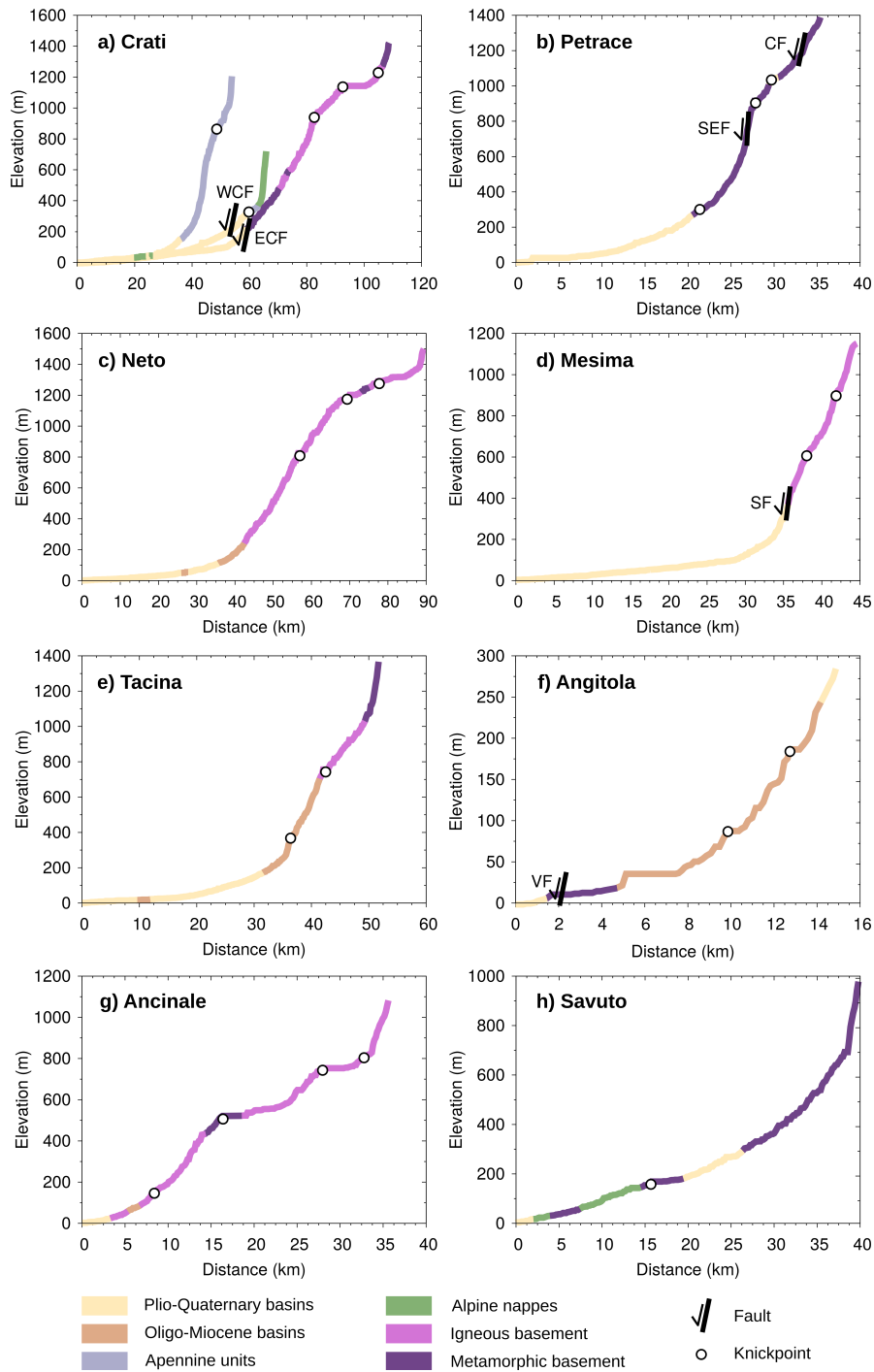


Figure 7. Longitudinal profiles showing positions of knickpoints and faults in the eight major drainage basins highlighted in Figure 5a. (a–h) Trunk streams (and other representative rivers for the Crati catchment) colored according to bedrock geology of Figure 1. WCF: West Crati Fault; ECF: East Crati Fault; CF: Citanova Fault; SEF: Santa Eufemia Fault; SF: Serre Fault; VF: Vibo Fault. Circles indicate knickpoints identified at abrupt breaks in channel slope not associated with large changes in upstream catchment area.

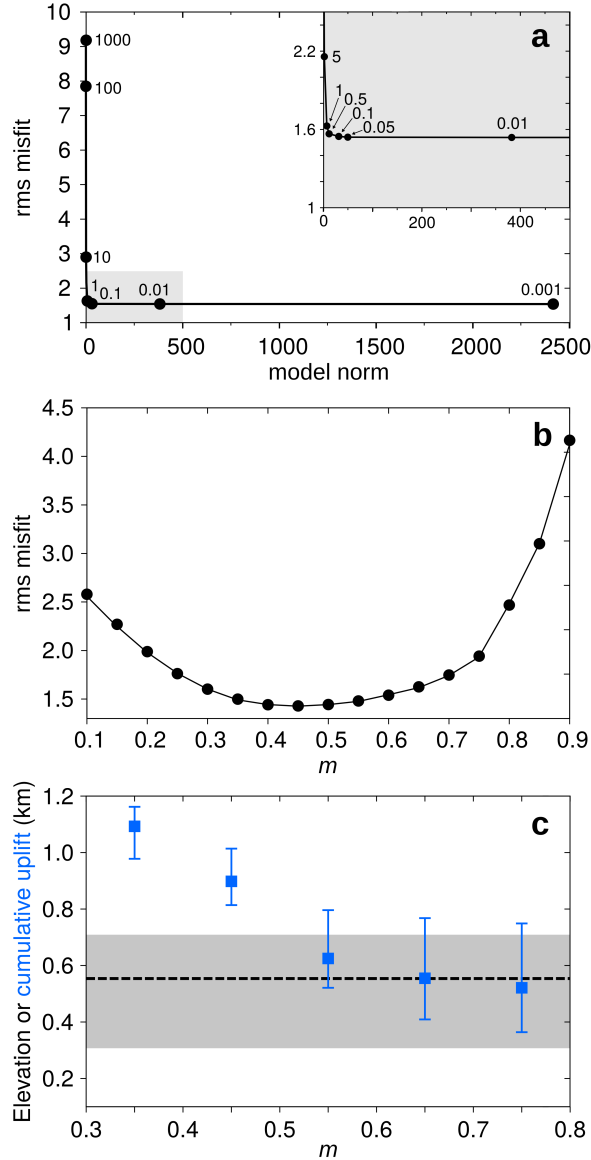


Figure 8. (a) Root mean squared (rms) misfit plotted against model norm for $m = 0.65$, labelled according to value of λ_s . Grey shaded region enlarged in inset. (b) Root mean squared (rms) misfit as a function of exponent of upstream area, m , for $\lambda_s = 1$. (c) Dashed line: mean elevation; grey polygon: minimum and maximum elevation for the upper terrace on the Capo Vaticano peninsula. Mean (blue squares) and range (blue error bars) of cumulative uplift on the Capo Vaticano peninsula predicted by fluvial inversion at 0 Ma ($\lambda_s = 1$).

478 lift is predicted from the model for the Sila Massif. More than 500 m of cumulative up-
 479 lift is observed on the Capo Vaticano peninsula by 72–108 ka, and uplift on the east coast
 480 of Calabria is typically less than 500 m throughout the model run. In the hanging wall
 481 of the Cittanova fault, and the northern Crati and Crotona basins, cumulative uplift does
 482 not exceed 300 m. Calculated uplift on the footwalls of the Serre and Cittanova faults
 483 is initially localised close to the centre of modern day fault traces (see 217 / 325 ka map
 484 in Figure 9). Significant cumulative footwall uplift is then observed along a greater ex-
 485 tent of the fault array in subsequent time steps.

486

3.1 Evaluation of fluvial inversion results

487

488

489

490

491

492

493

494

495

496

497

498

499

500

501

502

503

504

505

506

507

508

509

510

511

512

513

514

515

516

517

518

519

520

521

522

523

524

525

526

527

528

529

530

531

532

533

534

535

536

537

538

Given that we have used a simple stream power based erosion equation to model landscape evolution, are the uplift rates calculated from fluvial inverse modelling comparable to existing uplift rate estimates? The majority of uplift rates calculated from the model replicate, within error, uplift rates derived from Mid–Late Pleistocene terrace heights (Figure 11; Table 1). In Figure 11, a range of modeled uplift rates are presented (e.g. 1.6–2.2 mm yr⁻¹ for terrace ID = 10) because these ranges take into account the uncertainty in age of the oldest marine terrace (i.e. 0.8–1.2 Ma), which was used to calibrate erodibility, k , for the inverse model. The highest modeled uplift rate of 2.5 to 3.3 mm yr⁻¹ since MIS 5e coincides with highest observed uplift rate from a terrace on the Capo Vaticano peninsula (Table 1: ID = 14). The smallest uplift rate from the inversion model occurs on one of the lowest last interglacial terraces, near the town of Crotona (Table 1: ID = 34). The spatial variability in modeled uplift rate is similar to observed uplift rates measured on the Capo Vaticano peninsula and along the Tyrrhenian coastline.

The maximum cumulative uplift from the inverse model is 2077 m (Figure 9: 0 ka panel), situated on a vertex close to the northern drainage divide of the Crati catchment near Monte Pollino (2248 m). Large magnitudes of uplift (~ 1 km) are also predicted at the Sila, Serre and Aspromonte massifs during the youngest time steps (Figure 9). However, the fluvial inverse model assumes that all topography must be generated between 0.8–1.2 Ma and the present day, while the massifs probably had pre-existing relief of $\sim 10^2$ metres in the Sicilian stage, in contrast with the majority of Calabria (section 1.2). This may explain the high modeled uplift rates at the massifs since 100 ka. Uplift at the massifs is unlikely to be added at the start of the model because model coverage is very poor in these locations and at these time steps (Figure 9b).

In addition, we stress that the results presented here are based on the assumption that river erosion in Calabria can be approximated by a detachment-limited stream power model over the last ≈ 1 Myr. This assumption is probably valid for the majority of Calabria’s rivers, especially those in the south of the region that are actively incising across several faults with negligible sedimentation in the uplifting hanging walls (Figure 2). However, some low lying rivers, such as the those in the large Crati basin, presently contain alluvial channels close to the catchment mouth. Although we have few constraints on the long-term dynamics of these channels, the assumption of detachment limited erosion may not be appropriate in these areas. Consequently, we removed all rivers within the Crati catchment from the inverse model data as a test to investigate the potential effect of excluding these rivers on our results (Supplementary information and Figure S1a, b). However, the difference in predicted uplift between the model containing all rivers and the model without the Crati catchment generally does not exceed ± 30 m over a 200 to 300 kyr time interval (Supplementary Figure S1c). The uplift difference is usually less than ± 10 m in the areas containing the Cittanova and Serre faults and the dated marine terraces used to compare model and marine terrace uplift rates (Supplementary Figure S1). Consequently, we conclude that our results are not materially influenced by the inclusion of the Crati basin in our inverse model (further details provided in the Supplementary Information).

Finally, our analysis also assumes that slope exponent $n = 1$ in the stream power model. While there is ongoing discussion about the value of this exponent in a number of settings (e.g. Lague, 2014), we are encouraged that we obtain both a low residual misfit between the majority of longitudinal profiles and good spatial replication of uplift rate patterns denoted by Late Pleistocene marine terraces. We therefore suggest that a detachment-limited stream power model where $n = 1$ and $m = 0.65$ is appropriate to derive a plausible uplift history for Calabria over the last 1 Myr. We therefore proceed to analyse what the inverse model implies about the magnitude of regional uplift and the evolution of throw rates for Calabria’s faults, and we compare these insights with independent geological and geomorphic constraints.

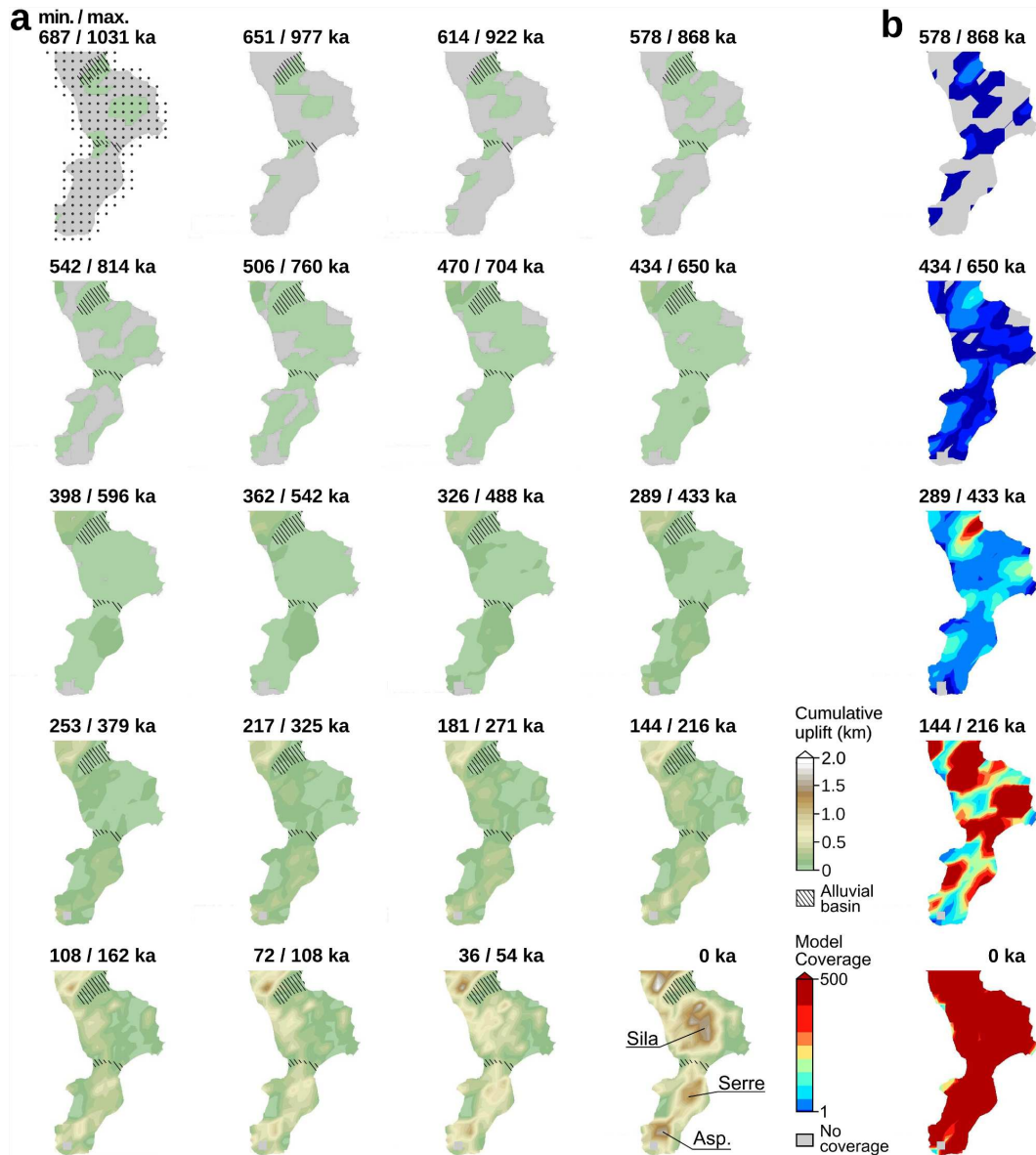


Figure 9. Cumulative uplift from best-fitting fluvial inverse model. (a) Predicted cumulative uplift maps. Gray circles = inversion model vertices (note 10 km spacing). Uplift rate is interpolated between these vertices along all rivers. Age ranges show propagated uncertainty from age of oldest marine terrace. Approximate locations of Sila, Serre and Aspromonte (Asp.) massifs indicated on 0 ka map. Hatched regions denote areas where a detachment limited erosional model may not be appropriate, based upon present day observations of alluvial basins.

539

3.2 Fault throw and regional uplift

540

541

542

543

544

545

The results from the inverse model provide an opportunity to analyse the temporal evolution of throw rate for the Serre and East Crati faults. The throw of these faults can be analysed using fluvial profiles because the thickness of hanging wall sediment is small (Roda-Boluda & Whittaker, 2017), as expected where hanging walls have experienced significant uplift. For instance, in the Crati basin, reflection seismic and well data indicate that Middle Pleistocene to Recent sediment thickness does not exceed 200 m

(Spina et al., 2011). For hanging wall sediment of negligible thickness, the difference in cumulative uplift between footwall and hanging wall approximates fault throw. Cumulative uplift from the inversion model was extracted from loci 5 km from the Serre and East Crati faults, in directions perpendicular to the fault traces, at locations where the oldest marine terrace is present in both footwall and hanging wall (Figure 12b and d). For the Serre fault, the most extensive footwall terraced area occurs on the southern part of the fault, while for the East Crati fault we could extract uplift from the fault centre (Figure 12b and d). We interpret the divergence of cumulative uplift at these loci as the onset of faulting. We initially discuss the results for $\lambda_s = 1$ (Figure 12), and results with damping parameter λ_s in the range 0.5 to 5 are included in Supplementary Information.

Divergence in cumulative uplift indicates that movement on the Serre fault began at approximately 650 ka if regional uplift initiates at 1 Ma (770 ka if regional uplift begins at 1.2 Ma; 510 ka if regional uplift begins at 0.8 Ma), which is 300 ka before movement on the East Crati fault (Figure 12). This result agrees with asynchronous fault initiation estimated from marine terraces offset by faults elsewhere in Calabria (e.g. Zecchin et al., 2004). The total amount of throw on the Serre (650 m) and East Crati (800 m) faults predicted from fluvial inverse modelling agrees well with stratigraphic observations and measurements of relief (Roda-Boluda & Whittaker, 2017), which also gives confidence to our results. We acknowledge that spatial damping of uplift rates in the model, determined by the value of λ_s , may affect the estimates of both fault initiation time and total throw magnitude. Results where the damping parameter λ_s is varied are presented in Supplementary Figure S2. These results show that reducing λ_s to 0.5 implies fault initiation at 400 ka for the East Crati Fault and 600 ka for the Serre fault (assuming initial uplift at 1 Ma). Apparent throw estimates for the present day are approximately 100 m larger than the equivalent interpretation if $\lambda_s = 1$, but still lie within the range predicted by independent data. Conversely, an increase in λ_s decreases the inferred age of fault initiation, and $\lambda_s = 5$ produces an unrealistically small throw magnitude for the East Crati fault (500 m).

Assuming uplift initiates at 1 Ma, average throw rates since the onset of faulting are 1.1 mm yr⁻¹ for the Serre fault and 2.3 mm yr⁻¹ for the East Crati fault (Figure 12), which are broadly consistent with previous estimates. The modeled throw rate on the Serre fault increases markedly at 100 ka (≈ 120 ka if regional uplift begins at 1.2 Ma; ≈ 80 ka if regional uplift begins at 0.8 Ma), which probably records the linkage of fault segments as inferred for many fault arrays in the Apennines and elsewhere (e.g. Faure Walker et al., 2009; Hopkins & Dawers, 2015). An increase in throw rate is also apparent in the $\lambda_s = 5$ and $\lambda_s = 0.5$ models (Supplementary Figure S2). Fluvial inverse modelling with initial uplift age of 1 Ma predicts a gradual increase in throw rate since ~ 0.3 Ma for the East Crati fault, which yields a similar throw rate to the Serre fault (≈ 4 mm yr⁻¹) when interpolated between 120–0 ka. The high throw rates predicted by the fluvial inverse model imply that there is a large seismic hazard in the region, and the rates are faster than those predicted from fault scarp trenching (≥ 0.44 mm yr⁻¹) for one strand of the Cittanova fault (Galli & Bosi, 2002). While the throw rates predicted by these methods are significantly different, they are not necessarily incompatible with each other. First, the comparison between uplift rates calculated from marine terraces and uplift rates predicted by the inverse model shows that uplift from the inverse model is generally only accurate within a factor of two (Figure 11), and when this uncertainty is taken into account the fault throw rates predicted by inverse modelling are consistent with those in the central Apennines (e.g. Morewood & Roberts, 2000; G. P. Roberts & Michetti, 2004). Second, the apparent discrepancy between the inverse model throw rates and the fault trenching throw rates may arise from temporal earthquake clustering (fault trenching throw rates are averaged over only 25 ka), spatial variation in slip along the fault array (fault trenching rates were obtained near the north tip of the Cittanova fault), or the assumptions used to estimate the initial uplift time in the inverse model (Galli & Bosi, 2002).

Catchment averaged erosion rates (0.35 mm yr⁻¹ for the southern tip of the Serre fault and 0.32 mm yr⁻¹ for the East Crati fault) are approximately an order of magni-

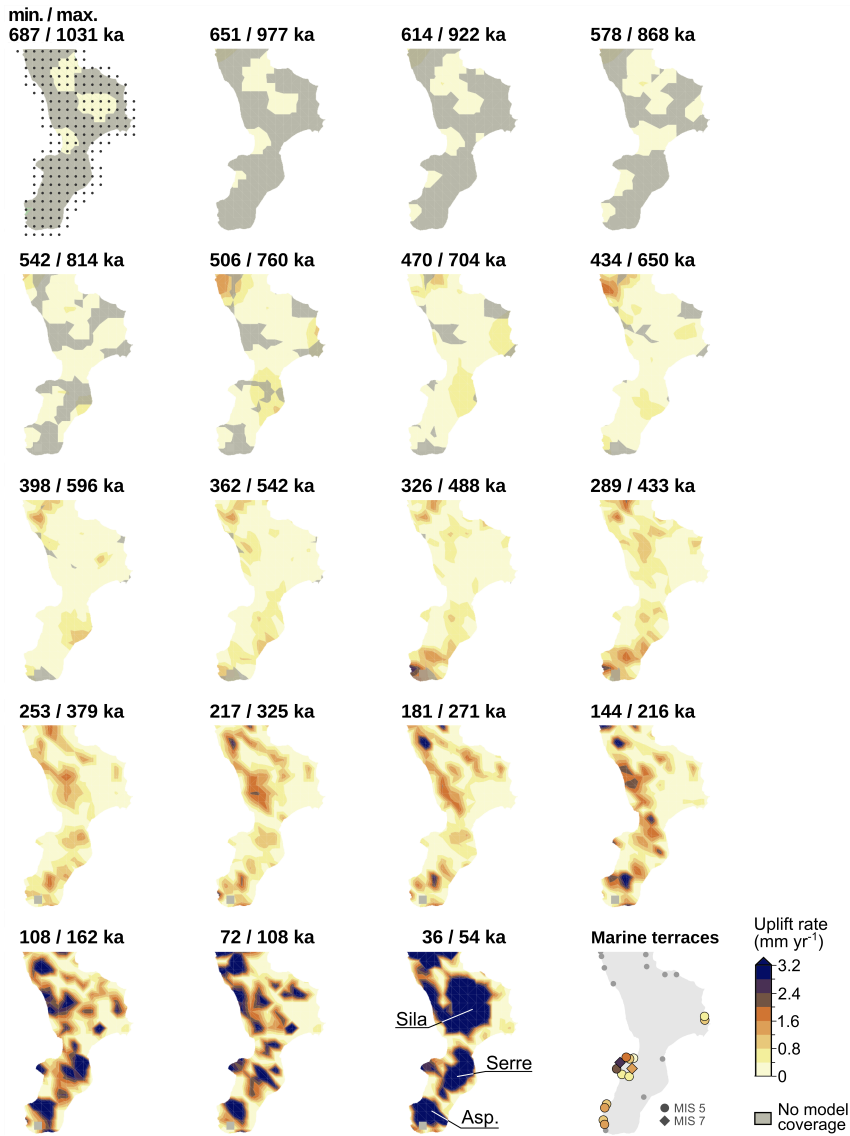


Figure 10. Uplift rates producing the best-fitting fluvial inverse model. Gray circles = inversion model vertices at 10 km vertical and horizontal separation. Age ranges show propagated uncertainty from age of oldest marine terrace (minimum age assumes uplift began at 0.8 Ma; maximum age assumes uplift began at 1.2 Ma). Marine terraces map produced using median uplift rates from independent observations in Table 1. Locations of Sila, Serre and Aspromonte (Asp.) massifs indicated on 36 / 54 ka map.

601 tude smaller than our predicted fault throw rates (Roda-Boluda et al., 2019). The large
 602 difference between the modeled uplift rates and erosion rates partially arises because the
 603 upstream reaches of many rivers have not reached equilibrium with recent uplift rates,
 604 so catchment averaged erosion rates may not balance uplift rates across the entire catch-
 605 ment. The difference between uplift rates and measured erosion rates may also reflect
 606 the different timescales of investigation. The mean integration time scales of the cosmo-
 607 genic nuclide erosion rates are 1.7 kyr and 1.9 kyr respectively (Roda-Boluda et al., 2018),
 608 while the fluvial inverse model only solves for uplift at 36 / 54 kyr time steps (Figures
 609 9 and 10) so cannot capture rapid fluctuations in erosion rate.

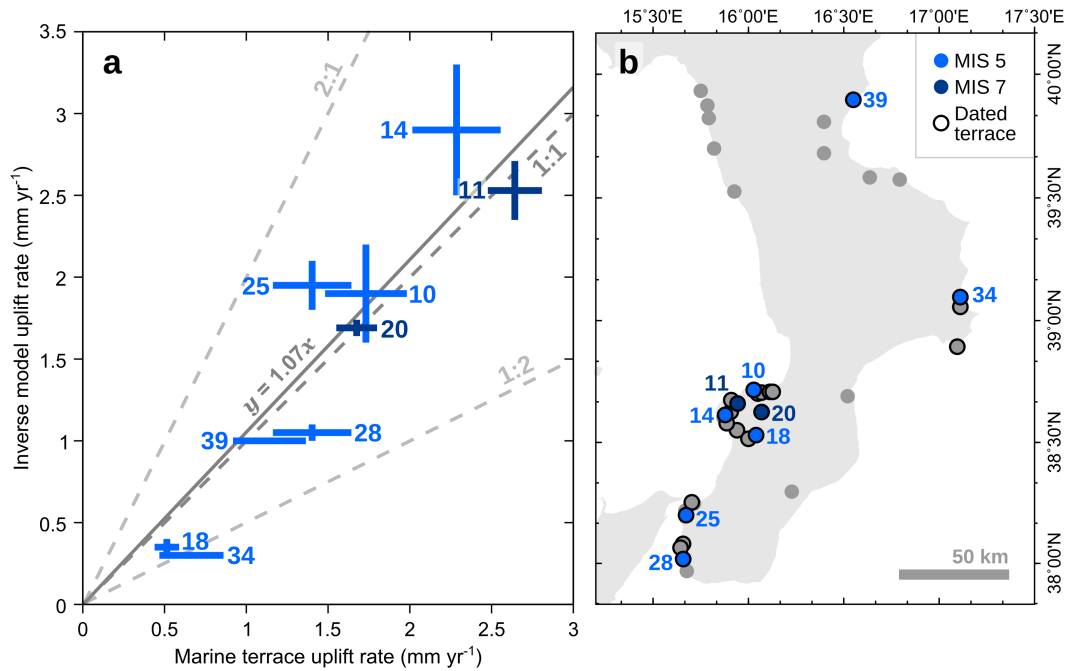


Figure 11. MIS 5 and MIS 7 uplift rates from dated terrace elevations and longitudinal profile inverse modelling. (a) Comparison between uplift rates derived from marine terrace elevations and uplift rates derived from fluvial inverse modelling for nine Mid–Late Pleistocene terrace locations. Terrace ID numbers refer to Table 1. Dashed lines denote theoretical 1:1, 2:1 and 1:2 ratios of uplift rates calculated from inverse modeling and marine terraces. Solid line represents linear regression, through the graph origin, between median uplift rates. (b) Map of Mid–Late Pleistocene terraces. Blue circles refer to the locations of MIS 5 and MIS 7 terraces used in this analysis. Locations enclosed in a black circle are all terraces with independent dating constraints (e.g. OSL, biostratigraphic correlation), which includes MIS 3 and Holocene terraces (Table 1).

610 Prior to ~ 0.6 Ma for the Serre fault, and ~ 0.3 Ma for the East Crati fault, similar
 611 uplift rates are observed in both the modern footwall and hanging wall. These results
 612 agree with suggestions of regional uplift preceding the onset of normal faulting in
 613 Calabria.

614 We will now use measured ratios of footwall uplift to hanging wall subsidence to
 615 calculate regional uplift using the methods in section 2.4. Terraces are present in both
 616 the footwall and proximal hanging wall of the Serre and East Crati faults, and the oldest
 617 terrace (Sicilian Stage, 0.8–1.2 Ma) can be correlated across the tip of the Serre fault,
 618 therefore regional uplift can be isolated using Equation 10. For Calabria, published estimates
 619 of the ratio of hanging wall subsidence to footwall uplift, α lie in the range 1 to
 620 2, with ≈ 1.6 calculated from observations on the Armo-Cittanova-Serre fault array (Roda-
 621 Boluda & Whittaker, 2017).

622 For values of α within the published range, the total amount of regional uplift calculated
 623 from the inversion model lies between 750 and 900 m, and modeled regional uplift
 624 rates increase through time for both the Serre and East Crati faults (Figure 12). Results
 625 show the same magnitude of regional uplift, within uncertainties calculated from the
 626 range of α , for both faults from 240 ka to the present.

627 The oldest terrace offset by the Cittanova fault is well preserved in both the foot-
 628 wall and in the hanging wall of the Piani d’Aspromonte (Figure 2a,b). Therefore, it is
 629 possible to estimate the total amount of cumulative uplift solely from terrace observa-

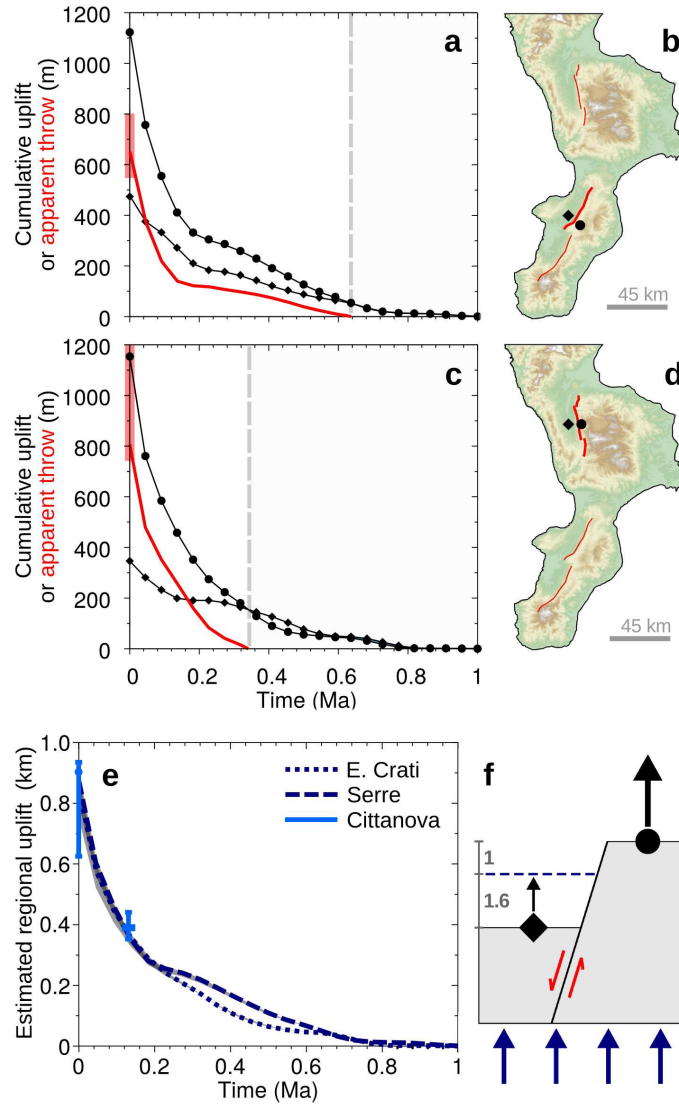


Figure 12. Fault-related and regional uplift derived from best-fitting inverse model with initial uplift at 1 Ma. (a) Modeled cumulative uplift of footwall (circles) and hanging wall (diamonds) of the Serre Fault. Red line: apparent throw (difference in uplift between footwall and hanging wall). Pink band: Geologic estimate of fault throw from Roda-Boluda & Whittaker (2017). Grey dashed line: Onset of fault movement inferred from first separation of model vertices in footwall and hanging wall. (b) Locations of vertices in panel (a). (c–d) Modeled uplift and fault throw for East Crati fault. (e) Calculated regional uplift assuming hanging wall subsidence to footwall uplift ratio $\alpha = 1.6$ (dashed lines) and α in the range 1 to 2 (grey shading). Light blue bars: Estimated regional uplift for the Cittanova fault at the present-day and for the last interglacial. (f) Modified version of Figure 4a. Dashed line represents the magnitude of regional uplift without fault movements, assuming $\alpha = 1.6$.

630 tions. Footwall elevation is the sum of regional uplift, Cittanova footwall uplift and a small
 631 amount of vertical motion from the nearby Santa Eufemia and Scilla faults. To estimate
 632 the magnitude of uplift generated by other faults, we subtracted the height of the foot-
 633 wall in the Petrace drainage basin, beyond the northern tip of the Santa Eufemia and

634 Scilla faults, from the height of the footwall at Aspromonte (Figure 2b). For simplicity,
 635 we assume that footwall uplift is similar along strike between these two locations (though
 636 uplift may have been greatest towards the centre of the footwall). Therefore, the mag-
 637 nitude of the regional uplift at the Cittanova fault, for α between 1 and 2, is 620–920 m
 638 (Figure 12). Footwall uplift since the last interglacial is extracted from the inversion model;
 639 hanging wall uplift over the same time period is the height of the marine terrace in the
 640 Petrace drainage basin (Pirrota et al., 2016).

641 The similar magnitude and rate of modeled regional uplift indicates that residual
 642 (i.e. non-fault related) uplift is broadly uniform across central Calabria between the Cit-
 643 tanova and East Crati faults (Figure 12). Such similarities are unlikely if apparent ob-
 644 servations of residual regional uplift result from the superposition of footwall uplift from
 645 multiple large normal faults.

646 A striking feature of our modeled regional uplift is the increase in regional uplift
 647 rate towards the present day, an increase which has also been suggested from a compar-
 648 ison of Holocene and MIS 5e marine terrace data (Antonioli et al., 2006). Although up-
 649 lift models derived from fluvial profile inversion cannot definitively identify the cause of
 650 landscape change, we can compare the spatial and temporal uplift calculated by the in-
 651 verse model to uplift patterns predicted by specific geological processes. Long wavelength
 652 regional uplift of Calabria has been attributed to processes either operating in the sub-
 653 lithospheric mantle, lower crustal flow or decoupling of the overriding and subducting
 654 plates (e.g. Gvirtzman & Nur, 1999; Wortel & Spakman, 2000; Westaway & Bridgland,
 655 2007; Faccenna et al., 2011). For example, Wortel and Spakman (2000) propose that a
 656 tear in the subducting slab, which has been imaged using p-wave tomography beneath
 657 southern Italy, could generate long-lived regional uplift due to rebound of the overriding
 658 plate. The timing of this slab tear probably coincides with the formation of oceanic
 659 crust in the Marsili basin between 1.6 and 2.1 Ma (Nicolosi et al., 2006; Guillaume et
 660 al., 2010), where oceanic spreading is indicative of an increase in stretching rate after
 661 narrowing of the subducting plate. The results from the inverse model suggest that re-
 662 gional uplift rates have increased towards the present-day which, assuming slab tear is
 663 complete, would be inconsistent with decreasing uplift rates predicted during rebound
 664 of the lithosphere to reach a new equilibrium elevation (e.g. Buiter et al., 2002). How-
 665 ever, we cannot rule out a time delay between detachment of the subducting slab and
 666 uplift of the overriding plate, which appears to depend on the depth of subduction (Duretz
 667 et al., 2011), or an additional, incipient slab tear of smaller magnitude that may be in-
 668 ferred from mantle seismicity (Maesano et al., 2017). Therefore, only multiple episodes
 669 of slab tear, or a time delay between slab tear and rebound would appear to account for
 670 the modeled increase in regional uplift rate.

671 However, toroidal mantle flow around the subducting slab beneath Calabria has
 672 also been inferred from shear wave splitting measurements (Civello & Margheriti, 2004),
 673 and predicted from seismic tomography, where it correlates well with high topography
 674 (Faccenna & Becker, 2010). Toroidal flow may generate continued uplift as long as roll-
 675 back operates, though its rate probably changes through time depending on the trench
 676 retreat velocity and plate width (Schellart, 2004; Piromallo et al., 2006). Moreover, toroidal
 677 flow may degrade the lithospheric thermal boundary layer (Zandt & Humphreys, 2008),
 678 which could produce uplift if the mantle lithosphere is thinned more than the crust (e.g.
 679 Esedo et al., 2012). While toroidal flow may be responsible for some uplift of the Cal-
 680 abrian Arc, could toroidal mantle flow account for the temporally increasing uplift rate
 681 predicted by Figure 12e? Extension of the lithosphere reduces its elastic thickness, which
 682 may make the overriding plate more susceptible to deformation caused by asthenospheric
 683 flow (e.g. d’Agostino et al., 2001). Therefore, Calabria may become more easily deformed
 684 by toroidal mantle flow as faults grow and interact over time, which could result in a tem-
 685 porally increasing regional uplift rate. We hypothesise that if stretching and thinning
 686 of the overriding plate has always occurred alongside regional uplift from asthenospheric
 687 flow, then the increase in uplift rate predicted by the inverse model could be consistent
 688 with ongoing toroidal mantle flow. Results from the inverse model may therefore em-

phasise the importance of considering geodynamic processes in both lithosphere and as-
 689 thenosphere, which is often neglected—or difficult to replicate—in numerical or phys-
 690 ical models.
 691

692 4 Conclusions

We have utilised a spatial and temporal inversion of 994 river longitudinal profiles
 693 to calculate uplift of Calabria, southern Italy. Erosion rates in a stream power model were
 694 calibrated using the age of the oldest marine terrace exposed throughout Calabria. Up-
 695 lift calculated by fluvial inverse modelling is consistent with uplift rates derived from dated
 696 last interglacial marine terraces, which indicates that a simple stream power equation
 697 can effectively model uplift and erosion in Calabria. Our results are consistent with vari-
 698 able uplift of Calabria since the Early Pleistocene from normal faults and regional pro-
 699 cesses, predicting 650 m and 800 m of total apparent throw on the Serre and East Crati
 700 faults, respectively. Fault throw calculated from fluvial inversion is consistent with in-
 701 dependent measurements of structural relief, and increases in throw rate are suggestive
 702 of fault interaction and linkage. Fluvial inversion, therefore, is shown to be a useful tech-
 703 nique to analyse fault array evolution. Non-fault related (i.e. regional) cumulative up-
 704 lift superimposed on three of Calabria’s major faults is responsible for ≈ 850 m of up-
 705 lift, and regional uplift rates appear to have increased towards the present day. An in-
 706 crease in regional uplift rate may indicate the combined effect of lithospheric weakness
 707 and ongoing mantle flow processes.
 708

709 Acknowledgments

This work was supported by a studentship from the Natural Environment Research Coun-
 710 cil (NERC) to JQS. River profiles are available from the National Geoscience Data Cen-
 711 tre (<https://dx.doi.org/10.5285/602a0a95-3541-408b-8ded-87d542d558e2>). The authors
 712 declare no conflicts of interest for this work.
 713

714 References

- 715 Antonioli, F., Ferranti, L., Fontana, A., Amorosi, A., Bondesan, A., Braitenberg,
 716 C., ... Stocchi, P. (2009). Holocene relative sea-level changes and vertical
 717 movements along the Italian and Istrian coastlines. *Quaternary International*,
 718 *206*(12), 102-133. doi: 10.1016/j.quaint.2008.11.008
- 719 Antonioli, F., Ferranti, L., Lambeck, K., Kershaw, S., Verrubbi, V., & Dai Pra, G.
 720 (2006). Late Pleistocene to Holocene record of changing uplift rates in south-
 721 ern Calabria and northeastern Sicily (southern Italy, Central Mediterranean
 722 Sea). *Tectonophysics*, *422*(1), 23-40. doi: 10.1016/j.tecto.2006.05.003
- 723 Attal, M., Cowie, P., Whittaker, A., Hobbey, D., Tucker, G., & Roberts, G. (2011).
 724 Testing fluvial erosion models using the transient response of bedrock rivers to
 725 tectonic forcing in the Apennines, Italy. *Journal of Geophysical Research*, *116*,
 726 F02005. doi: 10.1029/2010JF001875
- 727 Baccheschi, P., Margheriti, L., & Steckler, M. S. (2008). SKS splitting in Southern
 728 Italy: Anisotropy variations in a fragmented subduction zone. *Tectonophysics*,
 729 *462*(14), 49-67. doi: 10.1016/j.tecto.2007.10.014
- 730 Bianca, M., Catalano, S., De Guidi, G., Gueli, A. M., Monaco, C., Ristuccia, G. M.,
 731 ... Troja, S. O. (2011). Luminescence chronology of Pleistocene marine
 732 terraces of Capo Vaticano peninsula (Calabria, Southern Italy). *Quaternary*
 733 *International*, *232*(12), 114-121. doi: 10.1016/j.quaint.2010.07.013
- 734 Bishop, P., Hoey, T. B., Jansen, J. D., & Artza, I. L. (2005). Knickpoint recession
 735 rate and catchment area: the case of uplifted rivers in Eastern Scotland. *Earth*
 736 *Surface Processes and Landforms*, *30*(6), 767-778. doi: 10.1002/esp.1191
- 737 Boulton, S., Stokes, M., & Mather, A. (2014). Transient fluvial incision as an indi-

- 738 cator of active faulting and Plio-Quaternary uplift of the Moroccan High Atlas.
739 *Tectonophysics*, 633, 16-33. doi: 10.1016/j.tecto.2014.06.032
- 740 Braconnot, P., Otto-Bliesner, B., Harrison, S., Joussaume, S., Peterchmitt, J.-Y.,
741 Abe-Ouchi, A., . . . others (2007). Results of PMIP2 coupled simulations of the
742 Mid-Holocene and Last Glacial Maximum—Part 1: experiments and large-scale
743 features. *Climate of the Past*, 3(2), 261-277. doi: 10.5194/cp-3-261-2007
- 744 Braga, J. C., Martín, J. M., & Quesada, C. (2003). Patterns and average rates of
745 late Neogene-Recent uplift of the Betic Cordillera, SE Spain. *Geomorphology*,
746 50(1), 3-26. doi: 10.1016/S0169-555X(02)00205-2
- 747 Buiter, S. J., Govers, R., & Wortel, M. (2002). Two-dimensional simulations of
748 surface deformation caused by slab detachment. *Tectonophysics*, 354(3-4), 195-
749 210. doi: 10.1016/S0040-1951(02)00336-0
- 750 Capozzi, R., Artoni, A., Torelli, L., Lorenzini, S., Oppo, D., Mussoni, P., & Polonia,
751 A. (2012). Neogene to Quaternary tectonics and mud diapirism in the Gulf
752 of Squillace (Croton-Spartivento Basin, Calabrian Arc, Italy). *Marine and*
753 *Petroleum Geology*, 35(1), 219-234. doi: 10.1016/j.marpetgeo.2012.01.007
- 754 Carobene, L., & Dai Pra, G. (1990). Genesis, chronology and tectonics of the Qua-
755 ternary marine terraces of the Tyrrhenian coast of Northern Calabria (Italy).
756 Their correlation with climatic variations. *Il Quaternario*, 3(2), 75-94.
- 757 Catalano, S., De Guidi, G., Monaco, C., Tortorici, G., & Tortorici, L. (2008). Active
758 faulting and seismicity along the Siculo-Calabrian Rift Zone (Southern Italy).
759 *Tectonophysics*, 453(14), 177-192. doi: 10.1016/j.tecto.2007.05.008
- 760 Chiarabba, C., Jovane, L., & DiStefano, R. (2005). A new view of Italian seismic-
761 ity using 20 years of instrumental recordings. *Tectonophysics*, 395(3), 251-268.
762 doi: 10.1016/j.tecto.2004.09.013
- 763 Cinti, F., Alfonsi, L., D'Alessio, A., Marino, S., & Brunori, C. (2015). Fault-
764 ing and Ancient Earthquakes at Sybaris Archaeological Site, Ionian Cal-
765 abria, Southern Italy. *Seismological Research Letters*, 86(1), 245-254. doi:
766 10.1785/02201401071
- 767 Civello, S., & Margheriti, L. (2004). Toroidal mantle flow around the Calabrian slab
768 (Italy) from SKS splitting. *Geophysical Research Letters*, 31(10), L10601. doi:
769 10.1029/2004GL019607
- 770 Commins, D., Gupta, S., & Cartwright, J. (2005). Deformed streams reveal growth
771 and linkage of a normal fault array in the Canyonlands graben, Utah. *Geology*,
772 33(8), 645-648. doi: 10.1130/G21433AR.1
- 773 Conway-Jones, B. W., Roberts, G. G., Fichtner, A., & Hoggard, M. (2019). Neogene
774 epeirogeny of Iberia. *Geochemistry, Geophysics, Geosystems*, 20(2), 1138-1163.
775 doi: 10.1029/2018GC007899
- 776 Cowie, P., Gupta, S., & Dawers, N. (2000). Implications of fault array evolution for
777 synrift depocentre development: insights from a numerical fault growth model.
778 *Basin Research*, 12(3-4), 241-261. doi: 10.1111/j.1365-2117.2000.00126.x
- 779 Cowie, P., Phillips, R., Roberts, G., McCaffrey, K., Zijerveld, L., Gregory, L., . . .
780 Wilkinson, M. (2017). Orogen-scale uplift in the central Italian Apennines
781 drives episodic behaviour of earthquake faults. *Scientific Reports*, 7, 44858.
782 doi: 10.1038/srep44858
- 783 Cucci, L. (2004). Raised marine terraces in the Northern Calabrian Arc (South-
784 ern Italy): a 600 kyr-long geological record of regional uplift. *Annals of Geo-*
785 *physics*, 47(4). doi: 10.4401/ag-3350
- 786 Cucci, L., & Cinti, F. R. (1998). Regional uplift and local tectonic deformation
787 recorded by the Quaternary marine terraces on the Ionian coast of
788 northern Calabria (southern Italy). *Tectonophysics*, 292(1), 67-83. doi:
789 10.1016/S0040-1951(98)00061-4
- 790 Cyr, A. J., Granger, D. E., Olivetti, V., & Molin, P. (2010). Quantifying rock uplift
791 rates using channel steepness and cosmogenic nuclide-determined erosion rates:
792 Examples from northern and southern Italy. *Lithosphere*, 2(3), 188-198. doi:

- 793 10.1130/196.1
- 794 Czarnota, K., Roberts, G., White, N., & Fishwick, S. (2014). Spatial and tem-
795 poral patterns of Australian dynamic topography from River Profile Model-
796 ing. *Journal of Geophysical Research: Solid Earth*, *119*(2), 1384-1424. doi:
797 10.1002/2013JB010436
- 798 d'Agostino, N., Jackson, J., Dramis, F., & Funiciello, R. (2001). Interactions be-
799 tween mantle upwelling, drainage evolution and active normal faulting: an
800 example from the central Apennines (Italy). *Geophysical Journal Interna-*
801 *tional*, *147*(2), 475-497. doi: 10.1046/j.1365-246X.2001.00539.x
- 802 D'Arcy, M., & Whittaker, A. C. (2014). Geomorphic constraints on landscape sen-
803 sitivity to climate in tectonically active areas. *Geomorphology*, *204*, 366-381.
804 doi: 10.1016/j.geomorph.2013.08.019
- 805 Duretz, T., Gerya, T. V., & May, D. A. (2011). Numerical modelling of spontaneous
806 slab breakoff and subsequent topographic response. *Tectonophysics*, *502*(1-2),
807 244-256. doi: 10.1016/j.tecto.2010.05.024
- 808 Esedo, R., van Wijk, J., Coblenz, D., & Meyer, R. (2012). Uplift prior to conti-
809 nental breakup: Indication for removal of mantle lithosphere? *Geosphere*, *8*(5),
810 1078-1085. doi: 10.1130/GES00748.1
- 811 Faccenna, C., & Becker, T. (2010). Shaping mobile belts by small-scale convection.
812 *Nature*, *465*, 602-605. doi: 10.1038/nature09064
- 813 Faccenna, C., Becker, T. W., Auer, L., Billi, A., Boschi, L., Brun, J. P., ... Jolivet,
814 L. (2014). Mantle dynamics in the Mediterranean. *Reviews of Geophysics*,
815 *52*(3), 283-332. doi: 10.1002/2013RG000444
- 816 Faccenna, C., Molin, P., Orecchio, B., Olivetti, V., Bellier, O., Funiciello, F., ...
817 Billi, A. (2011). Topography of the Calabria subduction zone (southern
818 Italy): Clues for the origin of Mt. Etna. *Tectonics*, *30*(1), TC1003. doi:
819 10.1029/2010TC002694
- 820 Faure Walker, J., Roberts, G., Cowie, P., Papanikolaou, I., Sammonds, P., Michetti,
821 A., & Phillips, R. (2009). Horizontal strain-rates and throw-rates across
822 breached relay zones, central Italy: Implications for the preservation of throw
823 deficits at points of normal fault linkage. *Journal of Structural Geology*, *31*,
824 1145-1160. doi: 10.1016/j.jsg.2009.06.011
- 825 Faure Walker, J., Roberts, G. P., Cowie, P., Papanikolaou, I., Michetti, A., Sam-
826 monds, P., ... Phillips, R. (2012). Relationship between topography,
827 rates of extension and mantle dynamics in the actively-extending Ital-
828 ian Apennines. *Earth and Planetary Science Letters*, *325*, 76-84. doi:
829 10.1016/j.epsl.2012.01.028
- 830 Fellin, M. G., Zattin, M., Picotti, V., Reiners, P. W., & Nicolescu, S. (2005). Relief
831 evolution in northern Corsica (western Mediterranean): Constraints on uplift
832 and erosion on long-term and short-term timescales. *Journal of Geophysical*
833 *Research: Earth Surface*, *110*(F1), F0016. doi: 10.1029/2004JF000167
- 834 Ferranti, L., Antonioli, F., Mauz, B., Amorosi, A., Dai Pra, G., Mastronuzzi, G., ...
835 Radtke, U. (2006). Markers of the last interglacial sea-level high stand along
836 the coast of Italy: tectonic implications. *Quaternary international*, *145*, 30-54.
837 doi: 10.1016/j.quaint.2005.07.009
- 838 Ferranti, L., Oldow, J. S., D'Argenio, B., Catalano, R., Lewis, D., Marsella, E., ...
839 Pepe, F. (2008). Active deformation in southern Italy, Sicily and southern
840 Sardinia from GPS velocities of the Peri-Tyrrhenian Geodetic Array (PTGA).
841 *Bollettino della Società Geologica Italiana*, *127*(2), 299-316.
- 842 Fiannacca, P., Cirrincione, R., Bonanno, F., & Carciotto, M. M. (2015). Source-
843 inherited compositional diversity in granite batholiths: The geochemical mes-
844 sage of Late Paleozoic intrusive magmatism in central Calabria (southern
845 Italy). *Lithos*, *236-237*, 123-140. doi: 10.1016/j.lithos.2015.09.003
- 846 Ford, M., Rohais, S., Williams, E. A., Bourlange, S., Jousset, D., Backert,
847 N., & Malartre, F. (2013). Tectono-sedimentary evolution of the west-

- 848 ern Corinth rift (Central Greece). *Basin Research*, 25(1), 3-25. doi:
849 10.1111/j.1365-2117.2012.00550.x
- 850 Fossen, H., & Rotevatn, A. (2016). Fault linkage and relay structures in extensional
851 settings—A review. *Earth-Science Reviews*, 154, 14-28. doi: 10.1016/j.earscirev
852 .2015.11.014
- 853 Galli, P., & Bosi, V. (2002). Paleoseismology along the Cittanova fault: impli-
854 cations for seismotectonics and earthquake recurrence in Calabria (southern
855 Italy). *Journal of Geophysical Research: Solid Earth*, 107(B3), 2044. doi:
856 10.1029/2001JB000234
- 857 Galli, P., Galadini, F., & Pantosti, D. (2008). Twenty years of paleoseismology in
858 Italy. *Earth-Science Reviews*, 88(1), 89-117. doi: 10.1016/j.earscirev.2008.01
859 .001
- 860 Galli, P., Scionti, V., & Spina, V. (2007). New paleoseismic data from the Lakes and
861 Serre faults: seismotectonic implications for Calabria (Southern Italy). *Bollet-
862 tino della Società Geologica Italiana*, 126(2), 347-364.
- 863 Glotzbach, C. (2015). Deriving rock uplift histories from data-driven inversion of
864 river profiles. *Geology*, 43(6), 467-470. doi: 10.1130/G36702.1
- 865 Goren, L., Fox, M., & Willett, S. D. (2014). Tectonics from fluvial topography using
866 formal linear inversion: Theory and applications to the Inyo Mountains, Cal-
867 ifornia. *Journal of Geophysical Research: Earth Surface*, 119(8), 1651-1681.
868 doi: 10.1002/2014JF003079
- 869 Guillaume, B., Funiciello, F., Faccenna, C., Martinod, J., & Olivetti, V. (2010).
870 Spreading pulses of the Tyrrhenian Sea during the narrowing of the Calabrian
871 slab. *Geology*, 38(9), 819-822. doi: 10.1130/G31038.1
- 872 Gvirtzman, Z., & Nur, A. (1999). Plate detachment, asthenosphere upwelling, and
873 topography across subduction zones. *Geology*, 27(6), 563-566. doi: 10.1130/
874 0091-7613(1999)027<0563:PDAUAT>\$2.3.CO;2
- 875 Harel, M.-A., Mudd, S., & Attal, M. (2016). Global analysis of the stream power law
876 parameters based on worldwide ¹⁰Be denudation rates. *Geomorphology*, 268,
877 184-196. doi: 10.1016/j.geomorph.2016.05.035
- 878 Hopkins, M., & Dawers, N. (2015). Changes in bedrock channel morphology driven
879 by displacement rate increase during normal fault interaction and linkage.
880 *Basin Research*, 27, 43-59. doi: 10.1111/bre.12072
- 881 Howard, A. D. (1994). A detachment-limited model of drainage basin evolution.
882 *Water resources research*, 30(7), 2261-2285. doi: 10.1029/94WR00757
- 883 Howard, A. D., & Kerby, G. (1983). Channel changes in badlands. *Geological Society
884 of America Bulletin*, 94, 739-752. doi: 10.1130/0016-7606(1983)94<739:CCIB>2
885 .0.CO;2
- 886 Kirby, E., & Whipple, K. (2001). Quantifying differential rock-uplift rates
887 via stream profile analysis. *Geology*, 29(5), 415-418. doi: 10.1130/
888 0091-7613(2001)029<0415:qdrurv>2.0.co;2
- 889 Kirby, E., & Whipple, K. X. (2012). Expression of active tectonics in erosional land-
890 scapes. *Journal of Structural Geology*, 44, 54-75. doi: 10.1016/j.jsg.2012.07
891 .009
- 892 Lague, D. (2014). The stream power river incision model: evidence, theory and be-
893 yond. *Earth Surface Processes and Landforms*, 39, 38-61. doi: 10.1002/esp
894 .3462
- 895 Li, G., West, A. J., Densmore, A. L., Hammond, D. E., Jin, Z., Zhang, F., . . .
896 Hilton, R. G. (2016). Connectivity of earthquake-triggered landslides with
897 the fluvial network: Implications for landslide sediment transport after the
898 2008 Wenchuan earthquake. *Journal of Geophysical Research: Earth Surface*,
899 121(4), 703-724. doi: 10.1002/2015JF003718
- 900 Liberi, F., Morten, L., & Piluso, E. (2006). Geodynamic significance of ophiolites
901 within the Calabrian Arc. *Island Arc*, 15(1), 26-43. doi: 10.1111/j.1440-1738
902 .2006.00520.x

- 903 Loget, N., & Van Den Driessche, J. (2009). Wave train model for knickpoint migration.
904 *Geomorphology*, *106*(34), 376-382. doi: 10.1016/j.geomorph.2008.10.017
- 905 Maesano, F. E., Tiberti, M. M., & Basili, R. (2017). The Calabrian Arc: three-
906 dimensional modelling of the subduction interface. *Scientific Reports*, *7*, 8887.
907 doi: 10.1038/s41598-017-09074-8
- 908 Magni, V., Faccenna, C., van Hunen, J., & Funicello, F. (2014). How collision trig-
909 gers backarc extension: Insight into Mediterranean style of extension from 3-D
910 numerical models. *Geology*, *42*(6), 511-514. doi: 10.1130/G35446.1
- 911 Malinverno, A., & Ryan, W. B. (1986). Extension in the Tyrrhenian Sea and
912 shortening in the Apennines as result of arc migration driven by sinking of the
913 lithosphere. *Tectonics*, *5*(2), 227-245. doi: 10.1029/TC005i002p00227
- 914 Marc, O., Hovius, N., & Meunier, P. (2016). The mass balance of earthquakes and
915 earthquake sequences. *Geophysical Research Letters*, *43*(8), 3708-3716. doi: 10
916 .1002/2016GL068333
- 917 McLeod, A. E., Dawers, N. H., & Underhill, J. R. (2000). The propagation
918 and linkage of normal faults: insights from the Strathspey–Brent–Statfjord
919 fault array, northern North Sea. *Basin Research*, *12*(3-4), 263-284. doi:
920 10.1111/j.1365-2117.2000.00124.x
- 921 McNab, F., Ball, P. W., Hoggard, M. J., & White, N. J. (2018). Neogene Uplift
922 and Magmatism of Anatolia: Insights From Drainage Analysis and Basaltic
923 Geochemistry. *Geochemistry, Geophysics, Geosystems*, *19*(1), 175-213. doi:
924 10.1002/2017GC007251
- 925 Meschis, M., Roberts, G. P., Mildon, Z., Robertson, J., Michetti, A., &
926 Faure Walker, J. (2019). Slip on a mapped normal fault for the 28th De-
927 cember 1908 Messina earthquake (Mw 7.1) in Italy. *Scientific reports*, *9*(1),
928 6481. doi: 10.1038/s41598-019-42915-2
- 929 Miliareisis, G., & Paraschou, C. (2005). Vertical accuracy of the SRTM DTED level
930 1 of Crete. *International Journal of Applied Earth Observation and Geoinfor-
931 mation*, *7*, 49-59. doi: 10.1016/j.jag.2004.12.001
- 932 Minelli, L., & Faccenna, C. (2010). Evolution of the Calabrian accretionary
933 wedge (central Mediterranean). *Tectonics*, *29*(4), TC4004. doi: 10.1029/
934 2009TC002562
- 935 Mirabella, F., Brozzetti, F., Lupattelli, A., & Barchi, M. R. (2011). Tec-
936 tonic evolution of a low-angle extensional fault system from restored cross-
937 sections in the Northern Apennines (Italy). *Tectonics*, *30*(6), TC6002. doi:
938 10.1029/2011TC002890
- 939 Miyauchi, T., Dai Pra, G., & Sylos Labini, S. (1994). Geochronology of Pleis-
940 tocene marine terraces and regional tectonics in the Tyrrhenian coast of South
941 Calabria, Italy. *Il Quaternario*, *7*(1), 17-34.
- 942 Monaco, C., & Tortorici, L. (2000). Active faulting in the Calabrian arc and eastern
943 Sicily. *Journal of Geodynamics*, *29*(3-5), 407-424. doi: 10.1016/S0264-3707(99)
944 00052-6
- 945 Morewood, N. C., & Roberts, G. P. (2000). The geometry, kinematics and
946 rates of deformation within an en échelon normal fault segment bound-
947 ary, central Italy. *Journal of Structural Geology*, *22*(8), 1027-1047. doi:
948 10.1016/S0191-8141(00)00030-4
- 949 Mukul, M., Srivastava, V., Jade, S., & Mukul, M. (2017). Uncertainties in the
950 Shuttle Radar Topography Mission (SRTM) Heights: Insights from the In-
951 dian Himalaya and Peninsula. *Nature Scientific Reports*, *7*(41672). doi:
952 10.1038/srep41672
- 953 Nicolosi, I., Speranza, F., & Chiappini, M. (2006). Ultrafast oceanic spreading of
954 the Marsili Basin, southern Tyrrhenian Sea: Evidence from magnetic anomaly
955 analysis. *Geology*, *34*(9), 717-720. doi: 10.1130/g22555.1
- 956 Olivetti, V., Cyr, A. J., Molin, P., Faccenna, C., & Granger, D. E. (2012). Uplift
957 history of the Sila Massif, southern Italy, deciphered from cosmogenic ¹⁰Be

- erosion rates and river longitudinal profile analysis. *Tectonics*, 31(3). doi: 10.1029/2011TC003037
- 958
959
960 Palmentola, G., Acquafredda, P., & Fiore, S. (1990). A new correlation of the glacial
961 moraines in the Southern Apennines, Italy. *Geomorphology*, 3(1), 1-8. doi: 10
962 .1016/0169-555X(90)90028-O
- 963 Pantosti, D., Schwartz, D., & Valensise, G. (1993). Paleoseismology along the 1980
964 surface rupture of the Irpinia fault: implications for earthquake recurrence
965 in the southern Apennines. *Journal of Geophysical Research: Solid Earth*,
966 98(B4), 6561-6577. doi: 10.1029/92JB02277
- 967 Parker, R. L. (1977). Understanding inverse theory. *Annual Review of Earth and*
968 *Planetary Sciences*, 5, 35-64. doi: 10.1146/annurev.ea.05.050177.000343
- 969 Paul, J. D., Roberts, G. G., & White, N. (2014). The African landscape through
970 space and time. *Tectonics*, 33(6), 898-935. doi: 10.1002/2013TC003479
- 971 Pezzino, A., Angi, G., Fazio, E., Fiannacca, P., Lo Giudice, A., Ortolano, G., ...
972 De Vuono, E. (2008). Alpine metamorphism in the Aspromonte massif:
973 Implications for a new framework for the southern sector of the Calabria-
974 Peloritani orogen, Italy. *International Geology Review*, 50(5), 423-441. doi:
975 10.2747/0020-6814.50.5.423
- 976 Piromallo, C., Becker, T., Funiciello, F., & Faccenna, C. (2006). Three-dimensional
977 instantaneous mantle flow induced by subduction. *Geophysical Research Let-*
978 *ters*, 33(8), L08304. doi: 10.1029/2005GL025390
- 979 Piromallo, C., & Morelli, A. (2003). P wave tomography of the mantle under the
980 Alpine-Mediterranean area. *Journal of Geophysical Research: Solid Earth*,
981 108(B2), 2065. doi: 10.1029/2002JB001757
- 982 Pirrotta, C., Barbano, M. S., & Monaco, C. (2016). Evidence of active tectonics in
983 southern Calabria (Italy) by geomorphic analysis: the examples of the Catona
984 and Petrace rivers. *Italian Journal of Geosciences*, 135(1), 142-156. doi:
985 10.3301/IJG.2015.20
- 986 Pritchard, D., Roberts, G., White, N., & Richardson, C. (2009). Uplift histories
987 from river profiles. *Geophysical Research Letters*, 36(24), L24301. doi: 10
988 .1029/2009GL040928
- 989 Roberts, G. G., & White, N. (2010). Estimating uplift rate histories from river
990 profiles using African examples. *Journal of Geophysical Research: Solid Earth*,
991 115(B2), B02406. doi: 10.1029/2009JB006692
- 992 Roberts, G. G., White, N., Hoggard, M. J., Ball, P. W., & Meenan, C. (2018). A
993 Neogene history of mantle convective support beneath Borneo. *Earth and*
994 *Planetary Science Letters*, 496, 142-158. doi: 10.1016/j.epsl.2018.05.043
- 995 Roberts, G. G., White, N., Martin-Brandis, G., & Crosby, A. (2012). An up-
996 lift history of the Colorado Plateau and its surroundings from inverse
997 modeling of longitudinal river profiles. *Tectonics*, 31(4), TC4022. doi:
998 10.1029/2012TC003107
- 999 Roberts, G. P., Meschis, M., Houghton, S., Underwood, C., & Briant, R. M.
1000 (2013). The implications of revised Quaternary palaeoshoreline chronolo-
1001 gies for the rates of active extension and uplift in the upper plate of sub-
1002 duction zones. *Quaternary Science Reviews*, 78, 169-187. doi: 10.1016/
1003 j.quascirev.2013.08.006
- 1004 Roberts, G. P., & Michetti, A. (2004). Spatial and temporal variations in growth
1005 rates along active normal fault systems: an example from The Lazio - Abruzzo
1006 Apennines, central Italy. *Journal of Structural Geology*, 26, 339-376. doi:
1007 10.1016/S0191-8141(03)00103-2
- 1008 Robustelli, G. (2019). Geomorphic constraints on uplift history in the Aspromonte
1009 Massif, southern Italy. *Geomorphology*, 327, 319-337. doi: 10.1016/j.geomorph
1010 .2018.11.011
- 1011 Roda-Boluda, D. C., D'Arcy, M., McDonald, J., & Whittaker, A. (2018). Litholog-
1012 ical controls on hillslope sediment supply: insights from landslide activity and

- 1013 grain size distributions. *Earth Surface Processes and Landforms*, *43*, 956-977.
 1014 doi: 10.1002/esp.4281
- 1015 Roda-Boluda, D. C., D'Arcy, M., Whittaker, A. C., Gheorghiu, D. M., & Rodés, Á.
 1016 (2019). ¹⁰Be erosion rates controlled by transient response to normal faulting
 1017 through incision and landsliding. *Earth and Planetary Science Letters*, *507*,
 1018 140-153. doi: 10.1016/j.epsl.2018.11.032
- 1019 Roda-Boluda, D. C., & Whittaker, A. C. (2017). Structural and geomorpho-
 1020 logical constraints on active normal faulting and landscape evolution in
 1021 Calabria, Italy. *Journal of the Geological Society*, *174*(4), 701-720. doi:
 1022 10.1144/jgs2016-097
- 1023 Rodríguez Tribaldos, V., White, N. J., Roberts, G. G., & Hoggard, M. J. (2017).
 1024 Spatial and temporal uplift history of South America from calibrated drainage
 1025 analysis. *Geochemistry, Geophysics, Geosystems*, *18*(6), 2321-2353. doi:
 1026 10.1002/2017GC006909
- 1027 Rosenbaum, G., & Lister, G. S. (2004). Neogene and Quaternary rollback evolu-
 1028 tion of the Tyrrhenian Sea, the Apennines, and the Sicilian Maghrebides. *Tec-
 1029 tonics*, *23*(1), TC1013. doi: 10.1029/2003TC001518
- 1030 Rosenbaum, G., Lister, G. S., & Duboz, C. (2002). Reconstruction of the tectonic
 1031 evolution of the western Mediterranean since the Oligocene. *Journal of the
 1032 Virtual Explorer*, *8*, 107-130. doi: 10.3809/jvirtex.2002.00053
- 1033 Rossetti, F., Faccenna, C., Goffé, B., Monié, P., Argentieri, A., Funicello, R., &
 1034 Mattei, M. (2001). Alpine structural and metamorphic signature of the Sila
 1035 Piccola Massif nappe stack (Calabria, Italy): Insights for the tectonic evolution
 1036 of the Calabrian Arc. *Tectonics*, *20*(1), 112-133. doi: 10.1029/2000TC900027
- 1037 Rossetti, F., Goffé, B., Monié, P., Faccenna, C., & Vignaroli, G. (2004). Alpine oro-
 1038 genic P-T-t-deformation history of the Catena Costiera area and surrounding
 1039 regions (Calabrian Arc, southern Italy): The nappe edifice of north Calabria
 1040 revised with insights on the Tyrrhenian-Apennine system formation. *Tectonics*,
 1041 *23*(6). doi: 10.1029/2003TC001560
- 1042 Rovida, A. N., Locati, M., Camassi, R. D., Lolli, B., & Gasperini, P. (2016).
 1043 *CPTI15, the 2015 version of the Parametric Catalogue of Italian Earthquakes*.
 1044 Istituto Nazionale di Geofisica e Vulcanologia.
- 1045 Royden, L., & Perron, J. T. (2013). Solutions of the stream power equation and ap-
 1046 plication to the evolution of river longitudinal profiles. *Journal of Geophysical
 1047 Research: Earth Surface*, *118*(2), 497-518. doi: 10.1002/jgrf.20031
- 1048 Rudge, J. F., Roberts, G. G., White, N. J., & Richardson, C. N. (2015). Uplift
 1049 histories of Africa and Australia from linear inverse modeling of drainage in-
 1050 ventories. *Journal of Geophysical Research: Earth Surface*, *120*(5), 894-914.
 1051 doi: 10.1002/2014JF003297
- 1052 Savelli, C. (2002). Timespace distribution of magmatic activity in the western
 1053 Mediterranean and peripheral orogens during the past 30 Ma (a stimulus to
 1054 geodynamic considerations). *Journal of Geodynamics*, *34*(1), 99-126. doi:
 1055 10.1016/S0264-3707(02)00026-1
- 1056 Schellart, W. (2004). Kinematics of subduction and subduction-induced flow in the
 1057 upper mantle. *Journal of Geophysical Research*, *109*, B07401. doi: 10.1029/
 1058 2004JB002970
- 1059 Scicchitano, G., Antonioli, F., Berlinghieri, E. F. C., Dutton, A., & Monaco, C.
 1060 (2008). Submerged archaeological sites along the Ionian coast of southeast-
 1061 ern Sicily (Italy) and implications for the Holocene relative sea-level change.
 1062 *Quaternary Research*, *70*(1), 26-39. doi: 10.1016/j.yqres.2008.03.008
- 1063 Shen, Z., Dawers, N. H., Törnqvist, T. E., Gasparini, N. M., Hijma, M. P., & Mauz,
 1064 B. (2017). Mechanisms of late Quaternary fault throw-rate variability along
 1065 the north central Gulf of Mexico coast: implications for coastal subsidence.
 1066 *Basin Research*, *29*(5), 557-570. doi: 10.1111/bre.12184
- 1067 Siddall, M., Chappell, J., & Potter, E.-K. (2007). 7. Eustatic sea level during past

- 1068 interglacials. In F. Sirocko, M. Claussen, M. F. S. Goni, & T. Litt (Eds.), *The*
 1069 *climate of past interglacials* (Vol. 7, p. 75-92). Elsevier. doi: 10.1016/S1571
 1070 -0866(07)80032-7
- 1071 Siddall, M., Hönisch, B., Waelbroeck, C., & Huybers, P. (2010). Changes in
 1072 deep Pacific temperature during the mid-Pleistocene transition and Qua-
 1073 ternary. *Quaternary Science Reviews*, 29(1), 170-181. doi: 10.1016/
 1074 j.quascirev.2009.05.011
- 1075 Sklar, L., & Dietrich, W. E. (1998). River longitudinal profiles and bedrock
 1076 incision models: Stream power and the influence of sediment supply. In
 1077 K. Tinkler & E. Wohl (Eds.), *Rivers over rock: Fluvial processes in bedrock*
 1078 *channels* (Vol. 107, p. 237-260). American Geophysical Union. doi:
 1079 10.1029/GM107p0237
- 1080 Spina, V., Tondi, E., & Mazzoli, S. (2011). Complex basin development in a wrench-
 1081 dominated back-arc area: Tectonic evolution of the Crati Basin, Calabria,
 1082 Italy. *Journal of Geodynamics*, 51, 90-109. doi: 10.1016/j.jog.2010.05.003
- 1083 Stanley, J., & Bernasconi, M. P. (2012). Buried and submerged Greek archaeo-
 1084 logical coastal structures and artifacts as gauges to measure late Holocene
 1085 seafloor subsidence off Calabria, Italy. *Geoarchaeology*, 27(3), 189-205. doi:
 1086 10.1002/gea.21405
- 1087 Stock, J. D., & Montgomery, D. R. (1999). Geologic constraints on bedrock river
 1088 incision using the stream power law. *Journal of Geophysical Research: Solid*
 1089 *Earth*, 104(B3), 4983-4993. doi: 10.1029/98JB02139
- 1090 Stucky de Quay, G., Roberts, G., Watson, J., & Jackson, C. (2017). Incipient
 1091 mantle plume evolution: Constraints from ancient landscapes buried beneath
 1092 the North Sea. *Geochemistry, Geophysics, Geosystems*, 18(3), 973-993. doi:
 1093 10.1002/2016GC006769
- 1094 Tarboton, D. G. (1997). A new method for the determination of flow directions
 1095 and upslope areas in grid digital elevation models. *Water Resources Research*,
 1096 33(2), 309-319. doi: 10.1029/96WR03137
- 1097 Tortorici, L., Monaco, C., Tansi, C., & Cocina, O. (1995). Recent and active tecton-
 1098 ics in the Calabrian arc (Southern Italy). *Tectonophysics*, 243(1), 37-55. doi:
 1099 10.1016/0040-1951(94)00190-K
- 1100 Westaway, R. (1993). Quaternary Uplift of Southern Italy. *Journal of Structural Ge-*
 1101 *ology*, 98(B12), 21741-21772. doi: 10.1029/93JB01566
- 1102 Westaway, R., & Bridgland, D. (2007). Late Cenozoic uplift of southern Italy
 1103 deduced from fluvial and marine sediments: Coupling between surface pro-
 1104 cesses and lower-crustal flow. *Quaternary International*, 175, 86-124. doi:
 1105 10.1016/j.quaint.2006.11.015
- 1106 Whipple, K. X. (2004). Bedrock rivers and the geomorphology of active oro-
 1107 gens. *Annual Review of Earth and Planetary Science*, 32, 151-185. doi:
 1108 10.1146/annurev.earth.32.101802.120356
- 1109 Whipple, K. X., & Tucker, G. E. (1999). Dynamics of the stream-power river in-
 1110 cision model: Implications for height limits of mountain ranges, landscape
 1111 response timescales, and research needs. *Journal of Geophysical Research:*
 1112 *Solid Earth*, 104(B8), 17661-17674. doi: 10.1029/1999JB900120
- 1113 Whittaker, A. C. (2012). How do landscapes record tectonics and climate? *Litho-*
 1114 *sphere*, 4(2), 160-164. doi: 10.1130/RF.L003.1
- 1115 Whittaker, A. C., Attal, M., Cowie, P., Tucker, G., & Roberts, G. (2008). Decoding
 1116 temporal and spatial patterns of fault uplift using transient river long profiles.
 1117 *Geomorphology*, 100, 506-526. doi: 10.1016/j.geomorph.2008.01.018
- 1118 Whittaker, A. C., & Boulton, S. J. (2012). Tectonic and climatic controls on knick-
 1119 point retreat rates and landscape response times. *Journal of Geophysical Re-*
 1120 *search: Earth Surface*, 117(F2), F02024. doi: 10.1029/2011JF002157
- 1121 Whittaker, A. C., & Walker, A. S. (2015). Geomorphic constraints on fault
 1122 throw rates and linkage times: Examples from the Northern Gulf of Evia,

- 1123 Greece. *Journal of Geophysical Research: Earth Surface*, 120(1), 137-158. doi:
 1124 10.1002/2014JF003318
- 1125 Willett, S. D., McCoy, S. W., Perron, J. T., Goren, L., & Chen, C.-Y. (2014). Dy-
 1126 namic reorganization of river basins. *Science*, 343(6175), 1248765. doi: 10
 1127 .1126/science.1248765
- 1128 Wobus, C., Whipple, K., Kirby, E., Snyder, N., Johnson, J., Spyropolou, K., ...
 1129 Sheehan, D. (2006). Tectonics from topography: Procedures, promise, and
 1130 pitfalls. In S. Willett, N. Hovius, M. Brandon, & D. Fisher (Eds.), *Tectonics,*
 1131 *climate, and landscape evolution: Geological society of america special paper*
 1132 *398* (p. 55-74). Geological Society of America. doi: 10.1130/2006.2398(04)
- 1133 Wortel, M., & Spakman, W. (2000). Subduction and slab detachment in the
 1134 Mediterranean-Carpathian region. *Science*, 290(5498), 1910-1917. doi:
 1135 10.1126/science.290.5498.1910
- 1136 Zandt, G., & Humphreys, E. (2008). Toroidal mantle flow through the western U.S.
 1137 slab window. *Geology*, 36(4), 295-298. doi: 10.1130/G24611A.1
- 1138 Zecchin, M., Nalin, R., & Roda, C. (2004). Raised Pleistocene marine terraces
 1139 of the Crotona peninsula (Calabria, southern Italy): facies analysis and or-
 1140 ganization of their deposits. *Sedimentary Geology*, 172(12), 165-185. doi:
 1141 10.1016/j.sedgeo.2004.08.003
- 1142 Zhu, C., Byrd, R. H., Lu, P., & Nocedal, J. (1997). Algorithm 778: L-BFGS-B:
 1143 Fortran subroutines for large-scale bound-constrained optimization. *ACM*
 1144 *Transactions on Mathematical Software (TOMS)*, 23(4), 550-560. doi:
 1145 10.1145/279232.279236
- 1146 Zondervan, J. R., Whittaker, A. C., Bell, R. E., Watkins, S. E., Brooke, S. A., &
 1147 Hann, M. G. (2020). New constraints on bedrock erodibility and landscape
 1148 response times upstream of an active fault. *Geomorphology*, 351, 106937. doi:
 1149 10.1016/j.geomorph.2019.106937

Table 1. Calabria’s marine terraces and tidal notches with minimum–maximum average uplift rates since time indicated in the age column. Elevation errors from Ferranti et al. (2006). Uplift rates calculated using Equation 1 assuming MIS 5e occurred during 120–130 ka, with sea level 3–9 m above that of the present day (Ferranti et al., 2006). Paleo-sealevels and durations of other highstands from Siddall et al. (2007) and Siddall et al. (2010). H = Holocene. Dating method: TL = Thermoluminescence; OSL = Optically stimulated luminescence; SB = *Strombus bubonius*; SF = Senegalese fauna (not *S. bubonius*); RC = Radiocarbon (calibrated age used); AM = Aminoacid racimization. Assume terrace correlation if no dating method is given. [1] Antonioli et al. (2006); [2] Bianca et al. (2011); [3] Cucci (2004); [4] Cucci and Cinti (1998); [5] Ferranti et al. (2006); [6] G. P. Roberts et al. (2013).

ID	Long. (°)	Lat. (°)	Age (ka)	Dating method	Elevation (m)	Uplift rate (mm yr ⁻¹)	References
1	15.750	39.933			9.5 ± 0.1		5
2	15.785	39.874			7 ± 0.1		5
3	15.792	39.823			8 ± 8		5
4	15.820	39.700			10 ± 0.1		5
5	15.926	39.526			12 ± 0.1		5
6	16.127	38.708	MIS 7a (184 ± 20)	OSL	125	0.68–0.72	2
7(a)	16.112	38.708	MIS 5e (130 ± 8)	SB, U/Th	52 ± 20	0.18–0.58	5
7(b)	16.112	38.708	MIS 5e (121 ± 7)	SB, U/Th	50 ± 20	0.16–0.56	5
7(c)	16.106	38.707	MIS 5e (132 ± 1.6; 142 ± 1.8)	U/Th	50	0.32–0.39	6
8	16.069	38.705	MIS 5e (134 ± 13)	TL	153 ± 20	0.95–1.42	5
9	16.049	38.701	MIS 5e (128 ± 13)	TL	140 ± 20	0.93–1.39	5
10	16.028	38.716	MIS 5e	TL	216 ± 20	1.44–1.94	5
11 ¹	15.943	38.660	MIS 7c (207 ± 22)	OSL	560	2.48–2.81	2
12	15.910	38.674	MIS 5c (94 ± 8)	OSL	52	0.63–0.73	2
13	15.907	38.626	MIS 7c (199 ± 21)	OSL	465	2.19–2.32	2
14	15.878	38.613	MIS 5e	SF	285 ± 20	1.97–2.52	5
15	15.868	38.603			120 ± 20		5
16(a)	15.886	38.579	H (5.358 ± 0.1)	RC	1.8		1
16(b)	15.886	38.579	H (5.667 ± 0.08)	RC	1.8		1
17	15.940	38.550	MIS 5e	SB	90 ± 20	0.47–0.89	5
18	16.040	38.530	MIS 5e	SB	65 ± 4	0.40–0.55	5
19	16.000	38.515	MIS 3c (62 ± 6)	OSL	50		2
20	16.069	38.625	MIS 7e (214 ± 25)	OSL	380	1.55–1.80	2
21(a)	15.703	38.253	H (3.318 ± 0.103)	RC	2.9		1
21(b)	15.703	38.253	H (3.901 ± 0.105)	RC	2.9		1
21(c)	15.703	38.253	H (2.665 ± 0.164)	RC	2.5		1
21(d)	15.703	38.253	H (2.37 ± 0.105)	RC	2		1
22	15.715	38.248			125 ± 20		5
23	15.669	38.218			143 ± 20		5
24	15.671	38.208			170 ± 20		5
25	15.673	38.200	MIS 5e	TL	175 ± 20	1.12–1.60	5
26	15.657	38.081	MIS 5e (116 ± 13)	SB, TL, AM	129 ± 20	0.77–1.22	5
27	15.644	38.065	MIS 5e (116 ± 12)	SB, TL, AM	140 ± 20	0.85–1.31	5
28	15.658	38.018	MIS 5e	SB, AM	175 ± 20	1.12–1.60	5
29	15.677	37.968			146 ± 20		5
30	16.227	38.297			92 ± 20		5
31	16.520	38.690			104 ± 20		5
32	17.095	38.893	H (2.99 ± 0.05)	RC	0.6		1
33	17.111	39.056	MIS 5e (123)	SB, U/Th, AM	100 ± 20	0.55–0.98	5
34(a)	17.111	39.096	MIS 5e (142 ± 20)	SB, SF, TL	83 ± 20	0.42–0.83	5
34(b)	17.111	39.096	MIS 5e (149 ± 64)	SB, SF, TL	83 ± 20	0.42–0.83	5
35	16.793	39.574			130 ± 20		5
36	16.636	39.583			140 ± 20		5
37	16.396	39.681			135 ± 20		5
38	16.396	39.808			145 ± 20		5
39 ²	16.550	39.897	MIS 5e	AM	142 ± 20	0.87–1.33	3,4,5

¹This terrace was allocated to MIS 7e by Bianca et al. (2011) but we have re-allocated to MIS 7c, consistent with the OSL age.

²This terrace was only associated with correlation dating according to Ferranti et al. (2006), however we have included the AM dating, consistent with the primary data source of Cucci (2004).